UNIVERSITY OF CALIFORNIA

Los Angeles

Robust and Practical Beamforming for Millimeter-Wave Joint Communication and Sensing

A thesis submitted in partial satisfaction

of the requirements for the degree

Master of Science in Electrical and Computer Engineering

by

Dominic Kleinschmidt Olson

2026

ABSTRACT OF THE THESIS

Robust and Practical Beamforming for
Millimeter-Wave Joint Communication and Sensing

by

Dominic Kleinschmidt Olson
Master of Science in Electrical and Computer Engineering
University of California, Los Angeles, 2026
Professor Ian Roberts, Chair

As cellular networks continue to evolve toward the sixth-generation (6G) of wireless, joint communication and sensing (JCAS) has emerged as a promising research direction that aims to equip these communication networks with high-resolution sensing capabilities. Opportunities for JCAS are particularly ripe in systems operating at millimeter-wave (mmWave) frequencies, as they can offer both high range and angular resolution, courtesy of wide bandwidths and many antennas. Recent research aims to realize JCAS on such systems through a variety of innovative beamforming strategies, spanning compressive sensing, clutter rejection, interference cancellation, and others. Due to hardware imperfections, however, implementing these beamforming techniques on actual mmWave transceivers with high precision can be considerably difficult, but this has largely been overlooked in the majority of prior work on JCAS. In light of this, the objectives of this thesis are twofold. The first aim is to highlight the detrimental effects of these hardware imperfections on JCAS beamforming techniques, if not accounted for. The second aim is to propose methods to overcome these hardware imperfections through measurement and characterization of mmWave transceivers. To ac-

complish these objectives, extensive measurements are collected with a 60 GHz phased array platform using a custom signal processing pipeline. Then, this platform is used to experimentally evaluate two techniques proposed herein for physically realizing desired beams while accounting for hardware nonidealities. These experimental results indicate that the proposed techniques yield beams that tend to offer higher main lobe gain, lower side lobe levels, greater null depth, and reduced clutter, when compared to beams that neglect hardware impairments. Ultimately, the contributions of this thesis can be used to improve the translation of existing JCAS techniques to practice and can influence future research that involves high-precision beamforming on real-world transceivers.

The thesis of Dominic Kleinschmidt Olson is approved.

Yuanxun Wang

Danijela Cabric

Ian Roberts, Committee Chair

University of California, Los Angeles

2026

TABLE OF CONTENTS

LIST OF FIGURES

ACKNOWLEDGMENTS

I want to thank my advisor, Professor Ian Roberts, for his phenomenal guidance and continuous encouragement. I sincerely appreciate his valuable insights, thoughtful critiques, and willingness to make time for discussions throughout the duration of the work. His passion for the field has been a constant source of inspiration for me.

I also want to thank the members of my committee, Professor Danijela Cabric and Professor Yuanxun Ethan Wang, for their patience in reviewing and approving this thesis. Additional thanks goes to Professor Behzad Razavi and Dr. Sean Wang for an insightful discussion about beamformer circuits and their nonidealities.

I am particularly grateful for the support of Dr. Dennis M. Briggs. The opportunity to be a teaching assistant throughout my M.S. has been an unforgettable experience, helping me to grow as a person and serving as a frequent reminder of why I love EE.

I would like to express my gratitude to my labmates, Samuel Li, Jeong Min Kong, Sungho Cho, Kanishka Roy, Caden Davis, Ethan Ge, Hyunwoo Lee, Yunseo Lee, and Sunwoo Min, for their technical advice and for making the Wireless Lab a welcoming environment.

A special thanks goes to my classmates and friends, including but not limited to Benji Cruz, Cameron Fiske, Evan Bird, Jason Wu, Megan Chen, Taylor Kawate, Tiffany Chang, Sanjit Sarda, and Zayyir Ahmed, for their encouragement, motivation, and occasional much-needed distractions.

Lastly, I am grateful to my family for their love and support over all these years. I wouldn't be where I am today without them.

CHAPTER 1

Introduction

Next-generation radio systems with large bandwidths and many antennas are well-suited for joint communication and sensing (JCAS) applications, but implementing sophisticated beamforming techniques with high precision on real-world hardware can be a challenge. This thesis aims to bridge this gap between state-of-the-art beamforming research and its implementation on practical wireless platforms, with a particular emphasis on JCAS.

1.1 Background

Throughout the development of wireless technology, multi-antenna systems have been a major driver in performance improvements, as they can be used to increase signal-to-noise ratio (SNR), reduce interference, spatially multiplex data streams, and even communicate with multiple users at once. This trend has played out across many decades, from the conception of phased arrays to the proliferation of multiple-input multiple-output (MIMO) systems [1], and still continues today.

In recent times, two key innovations powering fifth-generation (5G) cellular networks include millimeter-wave (mmWave) communication and massive MIMO [2]. As applications evolve and enabling technologies and infrastructure continue to mature, mmWave systems and massive MIMO are all but certain to also play an important role in sixth-generation (6G) wireless networks and beyond [3].

Among efforts to define future 6G wireless technologies in recent years, joint communication and sensing (JCAS) has emerged as a particularly promising avenue with traction in academia, industry, and standardization bodies [4–6]. The core idea behind JCAS is to exploit mmWave and massive MIMO infrastructure for both high-speed wireless communication and high-resolution radar-like sensing, ideally using a single transceiver for both tasks. This capability is appealing to researchers and industry alike, as JCAS systems could make greater use of limited spectrum resources and could play a pivotal role in the proliferation of future cyber-physical systems [7].

Since wireless communication systems and radars typically employ similar but distinct hardware architectures, processing algorithms, and protocols, a key challenge in JCAS lies in designing and optimizing systems that exhibit good performance in both communication and sensing. Core to the vast majority of proposed JCAS techniques that address such challenges are innovative beamforming and/or waveform designs [8]. This thesis focuses on the beamforming aspect in particular, specifically within the context of mmWave systems.

The mmWave spectrum—ranging from roughly 30 GHz to 300 GHz—is remarkably attractive for JCAS, as it offers wide bandwidths, spanning up to several GHz, that can be used to attain fine range resolution. Additionally, since wavelengths are sub-centimeter at these frequencies, mmWave transceivers are typically equipped with tens or even hundreds of antenna elements within a reasonable footprint. These antenna arrays can provide fine angular resolution not usually encountered at lower frequencies. Finally, mmWave network deployments are typically much denser than lower-frequency cellular networks, with cell sizes on the order of 200 meters [9]. This density has the potential to enable unprecedented ubiquitous sensing on a network scale [10].

Recognizing this potential, multiple bodies of work have developed beamforming techniques for possible future 6G deployments with JCAS capabilities. One branch of research focuses on designing beams that steer lobes in multiple directions while minimizing clutter in other directions, creating carefully designed radiation patterns [11–14]. Another line of work centers on compressive sensing techniques [15], which exploit spatial sparsity in the high-dimensional mmWave setting. Finally, other work designs beams that place directional nulls [16] or perform interference cancellation in more sophisticated manners [17]. When considering typical monostatic systems where the transmitter and receiver are co-located, such as in a typical base station, strong self-interference can manifest between the two front-ends. Many strategies exist for mitigating this self-interference, including antenna isolation, analog cancellation, digital signal processing, and beamforming cancellation. These beamforming strategies utilize zero-forcing/nulling techniques [16, 18, 19] or more sophisticated optimization methods to design beams [20].

In spite of this promising work, important practical limitations and nonidealities impede the direct translation of proposed techniques to real-world systems. To start, most modern mmWave systems employ analog-only beamforming or hybrid beamforming architectures with substantially fewer radio frequency (RF) chains than antenna elements [21]. In these types of systems, element-wise gain and phase control is used to craft the beams, rather than the digital signal processing techniques employed in fully-digital beamforming, as shown in Figure 1.1. The use of analog beamforming greatly reduces power and hardware complexity, as fewer RF front-ends, data converters, and computational resources are required for a given antenna count. A primary drawback of analog beamforming is that it suffers from hardware imperfections, preventing a desired set of beamforming weights from being perfectly realized in hardware. If not attended to, these imperfections can cause deformations in the realized beam [22], including misshapen radiation patterns (e.g., more prominent sidelobes) [23] and shallower nulls [24]. These effects are largely ignored or not well diagnosed in the existing literature, preventing them from being accounted for during the development of beamforming techniques. While these effects can be negligible for simple objectives, such as steering a single beam in a desired direction, they can cause major issues in downstream tasks that exploit compressive sensing or rely on clutter reduction and interference cancellation.

Thus far, there is very little work that bridges the gap between sophisticated JCAS beamforming and real-world implementation. To improve the translation of JCAS research

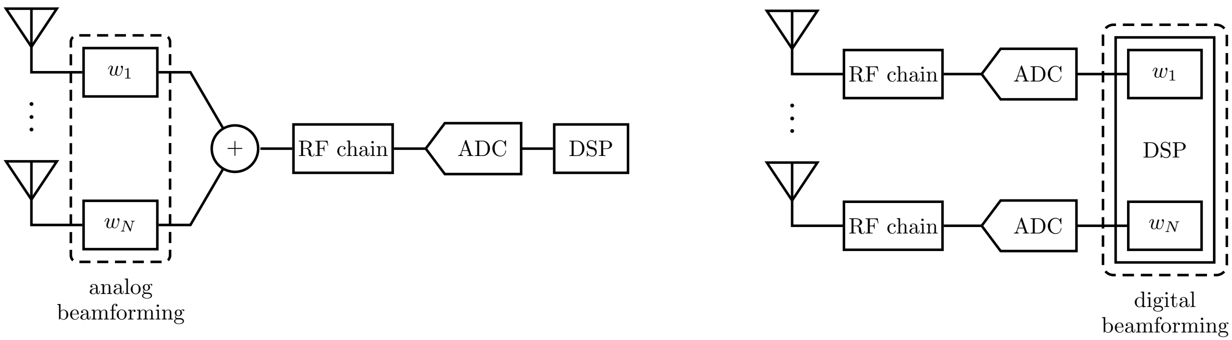

(a) Analog Beamformer.

(b) Digital Beamformer.

Figure 1.1: Comparison of (a) analog and (b) digital beamforming. In analog beamforming, gain and phase control of each element is done at RF, rather than in the digital domain.

to practice, the next generation of mmWave beamforming techniques should be evaluated, or perhaps explicitly designed, with specific characteristics of real hardware in mind. The overall aim of this work is to measure and analyze the effect of these imperfections, show where they emerge in a practical system, and demonstrate ways to overcome them.

1.2 Related Existing Work

In virtually any transceiver that employs analog beamforming, there arises the need to physically realize desired beamforming weights on the actual front-end, and this process is rarely trivial due to hardware limitations and nonidealities. Some research literature considers discrete, nonuniform phase control, presenting analytical [25, 26], heuristic [27], and measurement-based [28, 29] methods to design beams that maximize gain in a particular direction or over a given channel. While these methods are effective for maximizing gain with discrete phase control, they do not address more complicated objectives like the ones involved in JCAS, and do not generalize particularly well to the additional flexibility and complexity provided by arrays with both phase and amplitude control.

Other work does consider the commonly used vector modulator beamforming architecture that offers both phase and amplitude control [30], but makes an unrealistic assumption about vector modulator performance: that a uniform grid of amplitude and phase states can be produced [31, 32]. In practice, vector modulator performance is greatly affected by nonlinearity with respect to control setting and gain-dependent phase variation [33–36]. In contrast, characterization of similar imperfections of beamforming elements is considered in [37], but this considers a case where gain and phase can be independently controlled, a capability that mmWave systems, such as those with vector modulators, commonly do not have. Vector modulator performance characterization *in situ* is addressed in [38] but requires additional circuitry that is not present in any commercially available mmWave front-ends, to the author's knowledge.

Additional relevant work analyzes the effect of beam weight errors and quantization errors [22, 23] or optimizes for robustness against uncertainty [39]. However, they make assumptions about the error distribution (e.g., uniform or Gaussian) that do not accurately capture the aforementioned behavior of vector modulators. Importantly, they also do not leverage the fact that these imperfections can be measured, and thus incorporated into one's design.

Furthermore, despite these various efforts, most practical mmWave beamforming experiments do not actually make full use of the beamformer, but instead rely solely on a fraction of the possible beam settings. For instance, the Sivers phased arrays [40] used in a variety of wireless research [15, 41–46] have vector modulator phase shifters that can be set to 4096 possible states per element, but only a small codebook of 64 beams pointing in various directions is provided by the manufacturer. Some work only makes use of this codebook [41, 42], which is only suitable for cases where gain is maximized in one direction. Other work does deviate from the provided codebook, but does so in a constrained manner by relying on reinforcement learning to choose from a small subset of settings [45], or manually turning off antenna elements to realize sparse sensing rather than explicitly designing weights [15]. Other work also designs beams with the unrealistic assumption that the vector modulator is perfectly linear [46].

As illustrated by this thesis, greater capability can be extracted from the array by leveraging a full understanding of its settings, rather than relying on limited vendor information or assuming idealized behavior. This thesis examines the Sivers beamformer as a representative case study, and is, to the author's knowledge, the first published work that characterizes and exerts near-complete control over this particular front-end. This alone is expected to be a welcome contribution to the mmWave wireless research community, as it sheds much-needed light on these particular arrays, lowering the barrier to entry for others to use them, and paving the way for accurate real-world evaluation of sophisticated beamforming techniques. Beyond the Sivers arrays in particular, this thesis presents a framework for beamformer characterization and mapping beam weights to settings that are applicable to a wide variety of systems, including those not necessarily operating at mmWave frequencies.

1.3 Objectives and Outline

This thesis is organized as follows. First, in Chapter 2, a system model of mmWave phased arrays and their nonidealities is introduced. Following this, Chapter 3 presents strategies for effectively mapping desired beams to hardware settings, in spite of the nonidealities. Next, Chapter 4 describes the hardware setup and measurement procedures used for system characterization and experimental evaluation. Beamforming techniques pertinent to JCAS are then implemented on the phased array platform in Chapter 5, and the results are discussed. Finally, Chapter 6 concludes this thesis and discusses future work in this area.

CHAPTER 2

System Model

In this chapter, mathematical models of antenna arrays, beamforming, and vector modulators are laid forth, providing a foundation for the remainder of this thesis.

2.1 Analog Beamformer

In fully-analog beamforming, all array processing is conducted in the analog domain, with only one RF chain serving the entire antenna array. The analog beamforming network controls the amplitude and phase of a transmitted or received signal at each of the N antennas. A system illustration of analog transmit and receive beamformers with only one RF chain is shown in Figure 2.1. Since each of the N antennas has its own feed path and vector modulator, it is assumed each element will have its own distinct (but possibly related) nonidealities that need to be characterized.

2.2 Uniform Linear Array

For experimental viability, this work considers the uniform linear array (ULA) commonly employed in many systems [47–49], but is otherwise not tied to a particular array geometry. In a ULA, N antenna elements are arranged in a linear fashion such that adjacent elements are separated by a physical distance d, typically around half a wavelength $\lambda_{\mathrm{c}}/2$.

From the perspective of complex baseband, a plane wave impinging a ULA from the

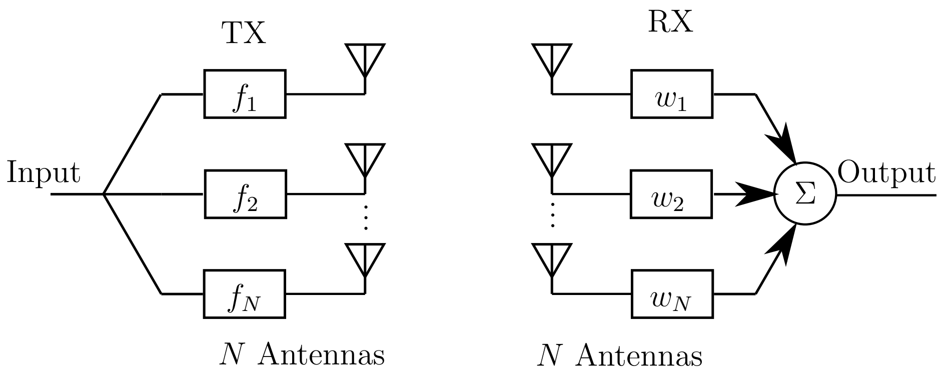

Figure 2.1: Functional block diagram of typical analog transmit and receive analog beamformers.

direction θ induces a phase shift at each of the N antennas. The phase shift experienced at the n-th element can be expressed as

$$a_n(\theta) = \mathrm{e}^{\mathrm{j}\frac{2\pi}{\lambda_c}(n-1)d\sin(\theta)}, \quad n = 1, 2, \ldots, N, \tag{2.1}$$

where $\theta = 0°$ corresponds to broadside of the array. Populating the response seen by all N antennas yields the array response vector

$$\boldsymbol{a}(\theta) = \begin{bmatrix} 1 \\ \mathrm{e}^{\mathrm{j}\frac{2\pi}{\lambda_c}1d\sin(\theta)} \\ \mathrm{e}^{\mathrm{j}\frac{2\pi}{\lambda_c}2d\sin(\theta)} \\ \vdots \\ \mathrm{e}^{\mathrm{j}\frac{2\pi}{\lambda_c}(N-1)d\sin(\theta)} \end{bmatrix}. \tag{2.2}$$

Using this, the array gain in some direction θ can be defined as

$$G(\theta) = \frac{|\boldsymbol{w}^*\boldsymbol{a}(\theta)|^2}{\sqrt{N}}, \tag{2.3}$$

where $\boldsymbol{w}$ is the beamforming weight vector whose n-th element w_n is the complex gain applied to the signal at the n-th antenna. Note that, in practice, analog beamforming happens on RF signals (at passband), meaning $\boldsymbol{w}$ represents the complex gain that is seen at baseband by the actual beamforming weights realized in hardware.

2.3 Array Calibration & Element Response

In an actual mmWave front-end, the antenna array and its feed may induce additional amplitude and phase variations *across elements*. Methods for correcting this phenomenon are known as *array calibration* and are well documented in phased array literature [28,46,50]. These variations across elements can be captured by the miscalibration vector $\boldsymbol{c} \in \mathbb{C}^N$, whose n-th entry represents the magnitude and phase variation of the n-th element. As shown in Section 4.6, this miscalibration vector can be determined from measurements and then accounted for during beamforming.

Additionally, the antenna elements in any given array are in general non-isotropic, and thus exhibit unique element patterns that can be captured by $e_n(\theta) \in \mathbb{C}$. These patterns can be stacked into an element response vector $\boldsymbol{e}(\theta)$. The combined effect of the miscalibration vector $\boldsymbol{c}$ and element response vector $\boldsymbol{e}(\theta)$ results in an effective array response $\tilde{\boldsymbol{a}}(\theta)$, defined by the elementwise multiplication

$$\tilde{\boldsymbol{a}}(\theta) = \boldsymbol{a}(\theta) \odot \boldsymbol{c} \odot \boldsymbol{e}(\theta), \tag{2.4}$$

which, as before, assumes no mutual coupling across elements.

When designing a beam $\boldsymbol{w}$, the the ideal array response $\boldsymbol{a}(\theta)$ can be used, and the effect of the element response $\boldsymbol{e}(\theta)$ can either be ignored or directly taken into account, depending on the objective of the particular technique to be employed. Then, to cancel out the effect of the miscalibration vector, $\tilde{\boldsymbol{w}}$ should be used to get the desired performance:

$$\tilde{\boldsymbol{w}} = \boldsymbol{w} \odot \boldsymbol{c}^{-1}, \tag{2.5}$$

where the inverse here is applied element-wise.

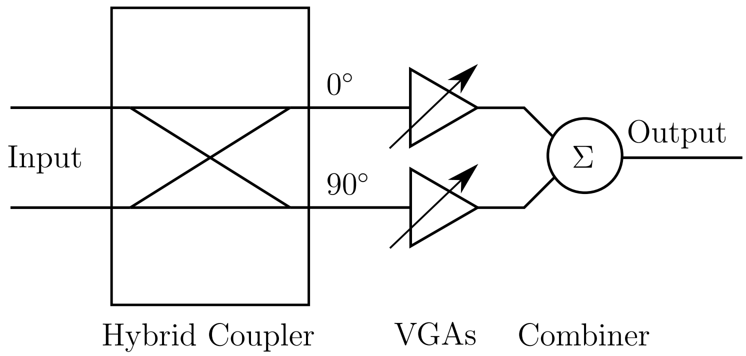

Figure 2.2: Functional schematic of a typical vector modulator phase shifter.

2.4 Vector Modulator Phase Shifter

As mentioned, a desired set of analog beamforming weights $\boldsymbol{w}$ are realized in hardware using RF circuitry, which can take a variety of forms. This work considers a vector modulator architecture in particular, as it is commonly used in mmWave front-ends [30], but the insights drawn herein could likely extend naturally to other beamforming architectures. A vector modulator consists of three stages: IQ generation, variable gain control, and vector summation. During IQ generation, the input signal is divided into two paths which differ in phase by 90°, using a hybrid coupler, for instance. Then, stepped gain control is applied to each path using variable gain amplifiers (VGAs) or variable attenuators with m bits of precision. Finally, the two signals are summed together using a combiner, for example. A block diagram depicting this process is shown in Figure 2.2.

The gain control elements in a vector modulator can be configured with settings i and q, adjusting the signed gain of $g_{\mathrm{I}}(i)$ and $g_{\mathrm{Q}}(q)$, respectively. Since i and q are discretely controlled with m bits of precision, they must be selected from a discrete set of $M = 2^m$

values, denoted by

$$\mathcal{M} = \{0, 1, \ldots, M-1\}. \tag{2.6}$$

Simply put, $i \in \mathcal{M}$ and $q \in \mathcal{M}$.

Reflected at complex baseband, the output of an *ideal* vector modulator whose input is $x(t)$ can be mathematically modeled as

$$y(t) = \left(g_{\mathrm{I}}(i) + \mathrm{j}\, g_{\mathrm{Q}}(q)\right) \cdot x(t), \tag{2.7}$$

where $g_{\mathrm{I}}(i)$ and $g_{\mathrm{Q}}(q)$ are purely real-valued and linear with respect to settings i and q, i.e.,

$$g_{\mathrm{I}}(i) = i - \frac{M-1}{2}, \tag{2.8}$$

$$g_{\mathrm{Q}}(q) = q - \frac{M-1}{2}. \tag{2.9}$$

When nonidealities are considered, these gains $g_{\mathrm{I}}(i)$ and $g_{\mathrm{Q}}(q)$ may deviate from this linear mapping and may in fact be complex-valued, as will be seen. This could be due to nonlinear control of the gain-tuning elements [51] and/or gain-dependent phase variations [36].

While this vector modulator architecture with sufficient control resolution can, in theory, produce a weight close to any desired one (up to a scaling factor) through an appropriate choice of i and q, a variety of nonidealities can complicate this process. For one, a phase imbalance between the I and Q paths may arise due to either imperfect IQ generation or path length differences. Furthermore, an amplitude imbalance can emerge due to differences in path attenuation or imperfect matching at the combiner. Together, these two issues can be understood as an *IQ imbalance* [52] with respect to $g_{\mathrm{I}}(i)$ and $g_{\mathrm{Q}}(q)$. Without loss of generality, this can be expressed as a gain difference $g_{\mathrm{imb}} \in \mathbb{R}$ and phase difference $\phi_{\mathrm{imb}} \in [0, 2\pi)$ between the I and Q paths. Capturing this, the revised input-output model is

$$y(t) = \left(g_{\mathrm{I}}(i) + \mathrm{j}\, g_{\mathrm{imb}} e^{\mathrm{j}\phi_{\mathrm{imb}}}\, g_{\mathrm{Q}}(q)\right) \cdot x(t), \qquad i, q \in \mathcal{M}, \tag{2.10}$$

which is the model considered henceforth in this thesis.

Note that this model assumes the I and Q paths to be completely independent. While this may not always be strictly true, it is experimentally observed that the coupling between the two paths only seems to have a noticeable effect on settings of high amplitude—which are seldom encountered in this work. It would be valuable future work to capture this coupling between the I and Q paths.

CHAPTER 3

Proposed Solutions

Typical beamforming designs implicitly assume a *continuous* set of possible beamforming weights, whereas only a discrete set of amplitude and phase settings are actually achievable with practical vector modulators. Therefore, to translate existing beamforming techniques to practice, it is necessary to use some scheme to quantize the weights, i.e., map them to settings of i and q. The simplest method, which is considered in this thesis, is to use a lookup table (LUT), denoted herein by the tensor $\boldsymbol{T} \in \mathbb{C}^{N \times M \times M}$, which stores each realizable weight across all antenna elements and vector modulator settings, with entries $T_{n,i,q}$ indexed by antenna element n, i setting, and q setting. Then, settings $\tilde{i}_n$ and $\tilde{q}_n$ for each weight w_n are chosen simply by projecting to the closest entry in $\boldsymbol{T}_{n,:,:}$ in the L_2 sense, while applying a scaling α and the array calibration c_n^{-1}, i.e.,

$$(\tilde{i}_n, \tilde{q}_n) = \underset{(i,q)}{\operatorname{argmin}} \ \left| T_{n,i,q} - \alpha \cdot c_n^{-1} \cdot w_n \right|, \tag{3.1}$$

with the resulting beamforming weight then *assumed* to be

$$\tilde{w}_n = T_{n,\tilde{i}_n,\tilde{q}_n}. \tag{3.2}$$

Recognize that the scaling factor α is constant for all n, meaning it merely scales the vector $\boldsymbol{w}$ but does not reshape it. Further, note that, upon setting the vector modulator at the n-th element to settings $(\tilde{i}_n, \tilde{q}_n)$, the realized beamforming weight will differ from this assumed value, unless the LUT $\boldsymbol{T}$ perfectly matches the true set of physically realizable settings. For this reason, the effectiveness of this strategy is greatly impacted by the specific LUT used—more specifically, how representative $\boldsymbol{T}$ is of the actual behavior of the vector modulators.

This chapter discusses approaches to two key design decisions for this process: namely, how to generate the LUT $\boldsymbol{T}$ used for quantization, and how to apply a scaling α to the beam weights $\boldsymbol{w}$ prior to the projection step to attain high gain without compromising performance.

3.1 Beam Setting Mapping

In this section, a baseline approach for populating the LUT $\boldsymbol{T}$ is introduced, along with two proposed approaches.

3.1.1 Linear LUT

Without any knowledge of the characteristics of the particular vector modulators or their nonidealities, the simplest way to design the LUT is to assume each element behaves like the ideal model described in (2.7). In this case, the real and imaginary parts of the complex weight scale linearly with the control setting as

$$T^{\mathrm{lin}}_{n,i,q} = g_{\mathrm{I}}(i) + \mathrm{j}\, g_{\mathrm{Q}}(q), \tag{3.3}$$

where

$$g_{\mathrm{I}}(i) = i - \frac{M-1}{2}, \tag{3.4}$$

$$g_{\mathrm{Q}}(q) = q - \frac{M-1}{2}. \tag{3.5}$$

This method neglects any IQ imbalance, control nonlinearity, and gain-dependent phase variation that may be present in practice, and is therefore expected to perform worse compared to cases when these factors are taken into account.

3.1.2 Measured LUT

The first LUT proposed herein improves upon the linear LUT by explicitly measuring each setting to account for nonidealities that may be present. To fully characterize the vector modulator at each antenna, one can explicitly measure every possible setting to populate each entry of a LUT denoted by $\boldsymbol{T}^{\text{meas}}$. A measurement procedure to accomplish this is described in Chapter 5.

In theory, measuring each possible state of each vector modulator would presumably be optimal, but there are challenges with this approach. First and foremost, collecting measurements to populate the entirety of $\boldsymbol{T}^{\text{meas}}$ can be time consuming, since a vector modulator with m bits of I and Q control has $M^2 = 2^{2m}$ possible settings and these settings must be measured sequentially. This is exacerbated by the presence of thermal noise, oscillator phase noise, DC offsets, and other issues which introduce measurement error, since multiple (sometimes many) measurements are needed to reduce estimation error. These issues motivate the need to characterize vector modulator phase shifters *without measuring every setting* by exploiting the structure of the vector modulator. This motivates the approach introduced next.

3.1.3 Fit LUT

The process of measuring every setting of a single vector modulator requires $\mathcal{O}(M^2)$ time. However, with knowledge of the vector modulator architecture, it is shown that it is possible to characterize it well in $\mathcal{O}(M)$ time using the following approach.

As discussed in Section 2.4, vector modulators are susceptible to IQ imbalance, nonlinear amplitude control, and gain-dependent phase variation. In this approach, each of the N vector modulators are considered separately, assuming that any interaction between any two is negligible. First, the IQ imbalance of each vector modulator is explicitly estimated, and then the nonlinear complex gain functions $g_{\text{I}}(i)$ and $g_{\text{Q}}(q)$ with respect to each control setting i or q are estimated and stored. An approach to estimating these quantities is summarized next.

Two values are needed to correct IQ imbalance: the gain imbalance, denoted by g_{imb}, and

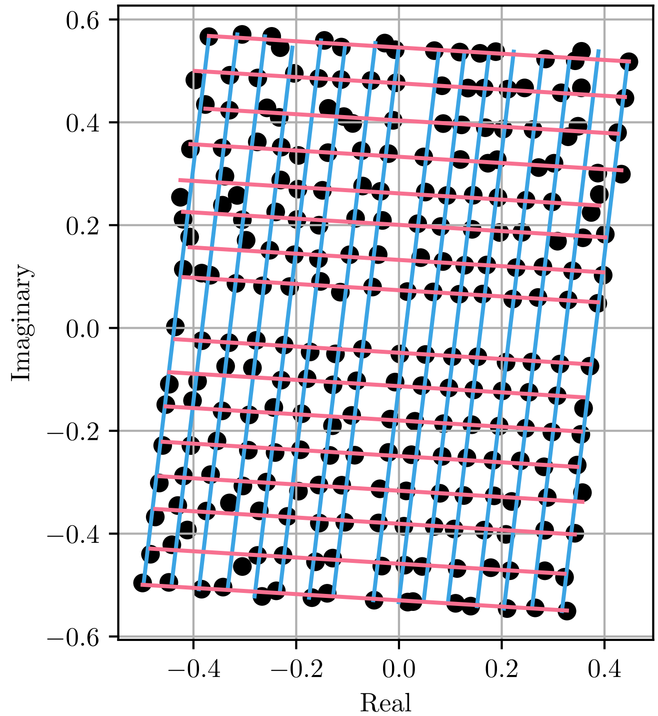

Figure 3.1: Linear grid fit of the innermost $(2C)^2$ measured settings (the values contained in $\boldsymbol{T}^{\text{meas}}_{n,\mathcal{M}_C,\mathcal{M}_C}$) of the vector modulator at a single antenna element n, where $C = 8$. Using this fit, the values can be properly zero-centered and the variation across i and q can be orthogonalized by correcting for the observed IQ imbalance.

the phase deviation from a perfect 90° offset, denoted by ϕ_{imb}. To isolate the IQ imbalance, points with minimal amplitude nonlinearity and gain-dependent phase variation should be used, which are observed to be the innermost $2C$ amplitude settings for both i and q, i.e., the set:

$$\mathcal{M}_C = \left\{ \frac{M}{2} - C, \ldots, \frac{M}{2} + C - 1 \right\}. \tag{3.6}$$

As such, the values in the submatrix $\boldsymbol{T}^{\text{meas}}_{n,\mathcal{M}_C,\mathcal{M}_C}$ can be used for IQ imbalance estimation. The slopes a_{I}, a_{Q} and intercepts $\boldsymbol{b}_{\text{I}}$, $\boldsymbol{b}_{\text{Q}}$ of the grid formed by these inner settings, i.e., for either i or q fixed,

$$\Re(\boldsymbol{T}^{\text{meas}}_{n,\mathcal{M}_C,q}) = a_{\text{I}} \cdot \Im(\boldsymbol{T}^{\text{meas}}_{n,\mathcal{M}_C,q}) + b_{\text{I},q} \tag{3.7}$$

$$\Im(\boldsymbol{T}^{\text{meas}}_{n,i,\mathcal{M}_C}) = a_{\text{Q}} \cdot \Re(\boldsymbol{T}^{\text{meas}}_{n,i,\mathcal{M}_C}) + b_{\text{Q},i} \tag{3.8}$$

can be estimated using least squares. An example of this is shown in Figure 3.1. These slopes and intercepts can then be used to center the points and calculate the IQ imbalance parameters via

$$g_{\text{imb}} = \frac{1}{2C} \sum_{k=\frac{M}{2}-C}^{\frac{M}{2}+C} \frac{b_{\text{I},k} - \frac{1}{2C}\sum_{q=\frac{M}{2}-C}^{\frac{M}{2}+C} b_{\text{I},q}}{b_{\text{Q},k} - \frac{1}{2C}\sum_{q=\frac{M}{2}-C}^{\frac{M}{2}+C} b_{\text{Q},q}} \tag{3.9}$$

$$\phi_{\text{imb}} = \arctan(a_{\text{Q}}) - \arctan(1/a_{\text{I}}) - 90^\circ. \tag{3.10}$$

An IQ imbalanced version $\hat{y}$ of a variable y can be expressed as [52]

$$\hat{y} = y + \kappa y^*, \tag{3.11}$$

where

$$\kappa = \frac{1 - g_{\text{imb}} \mathrm{e}^{\mathrm{j}\phi_{\text{imb}}}}{1 + g_{\text{imb}} \mathrm{e}^{-\mathrm{j}\phi_{\text{imb}}}}. \tag{3.12}$$

Rearranging (3.11) to solve for y leads to

$$y = \frac{\hat{y} - \kappa \hat{y}^*}{1 - \kappa^2} \tag{3.13}$$

which illuminates how to correct IQ imbalance once it has been estimated.

Once the i and q settings have been completely orthogonalized by correcting for IQ imbalance, the magnitude and phase contributions of the I and Q branch can be analyzed separately, using averages across the other setting. For instance, IQ-corrected versions of the intercepts $\boldsymbol{b}_{\text{I}}$ can be subtracted from the data points in $\boldsymbol{T}^{\text{meas}}_{n,:,\mathcal{M}_C}$ to overlay points from $2C$ settings of q across all M values of i. Then, $|g_{\text{I}}(i)|$ can be estimated for each value of i by taking the magnitude and averaging across q. This process is shown in Figure 3.2. A similar

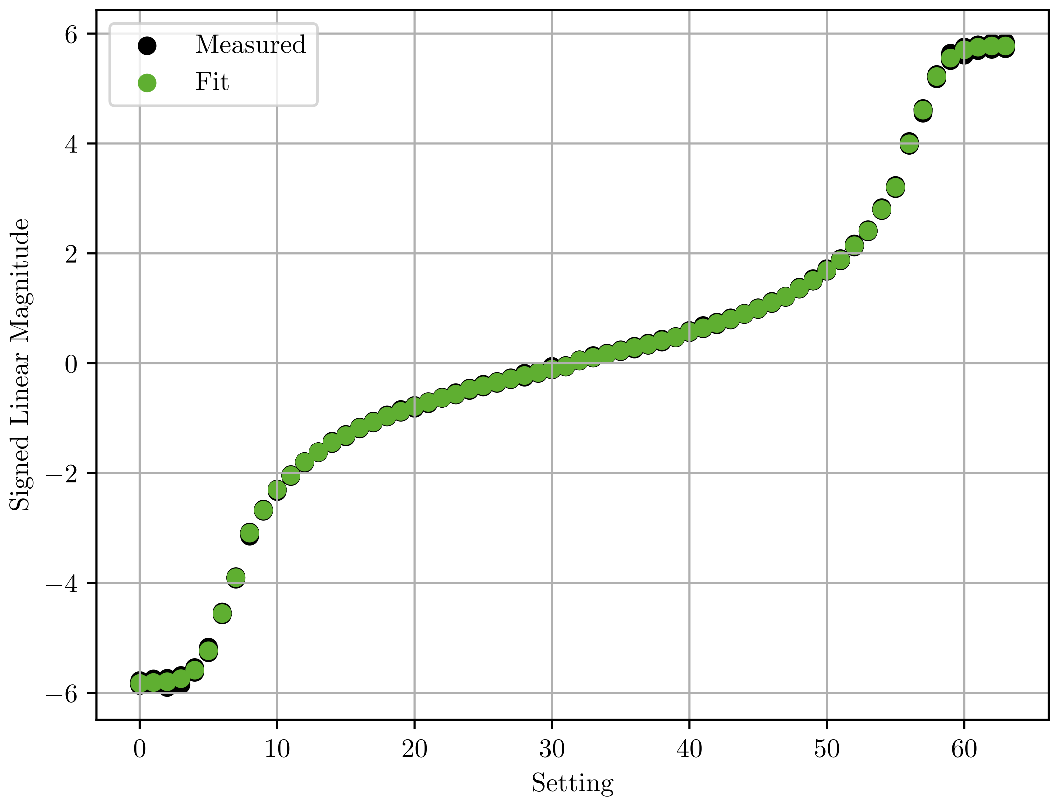

Figure 3.2: Magnitude variation across all values of i, for several values of q, with the average shown in green.

process can be used for $\angle g_{\mathrm{I}}(i)$, but phase noise during actual measurements has proven too severe to rely on an average alone. Instead, one can explicitly set the phase of all the middle settings to zero—as it is assumed there is no gain-dependent phase variation there—take an average everywhere else, and apply a moving-average filter, i.e.,

$$\angle g_{\mathrm{I}}(i) = \frac{1}{2K+1} \sum_{k=-K}^{K} \angle g_{\mathrm{I,avg}}(i-k). \tag{3.14}$$

The result of this operation is shown in Figure 3.3. The same process can be used to get $|g_{\mathrm{Q}}(q)|$ and $\angle g_{\mathrm{Q}}(q)$. These functions can then be used to generate the complete LUT of all

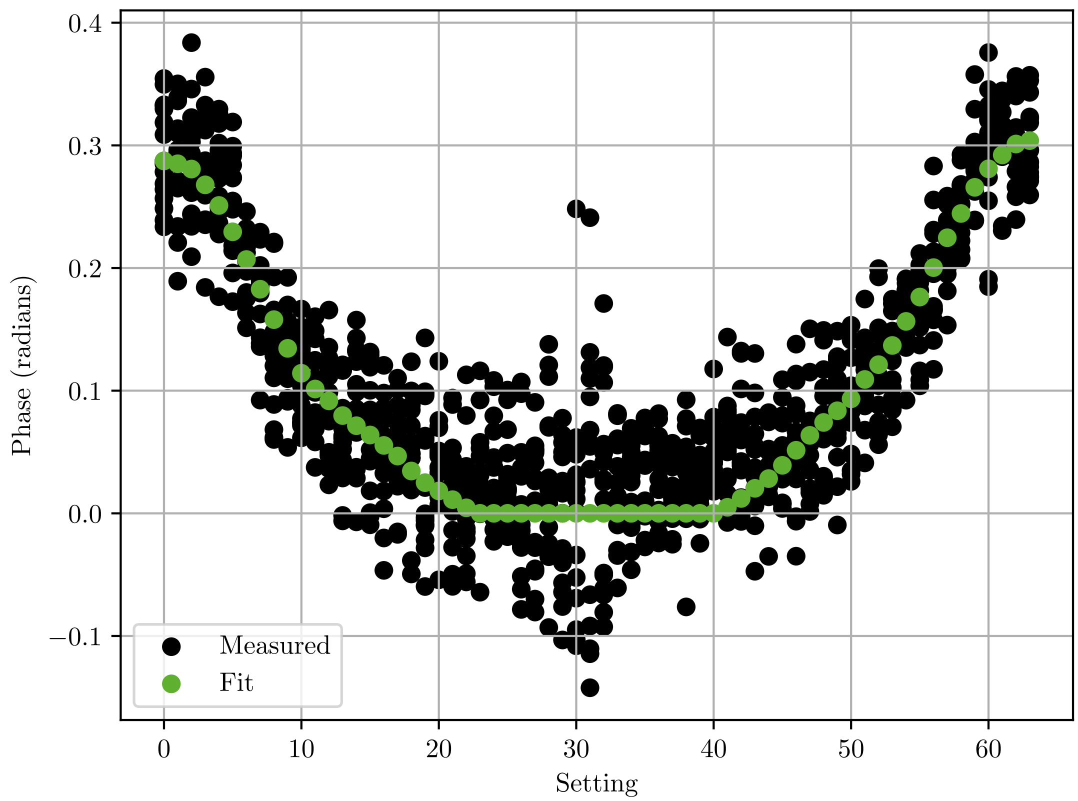

Figure 3.3: Phase variation across all values of i, for several values of q, with a fit performed using an average, clipping all low-amplitude settings to zero phase, and applying a moving-average filter.

settings, while reintroducing the IQ imbalance, via the equation

$$T^{\mathrm{fit}}_{n,i,q} = \big(g_{\mathrm{I}}(i) + \mathrm{j}\, g_{\mathrm{imb}} \mathrm{e}^{\mathrm{j}\phi_{\mathrm{imb}}}\, g_{\mathrm{Q}}(q)\big). \tag{3.15}$$

Note that this approach only requires a fraction of the total LUT to be explicitly measured, with the remaining entries populated based on the behavior inferred from these measurements.

The result of this process is illustrated in Figure 3.4, showing good alignment between the measured and fit LUT, aside from some of the outermost corner settings—which are

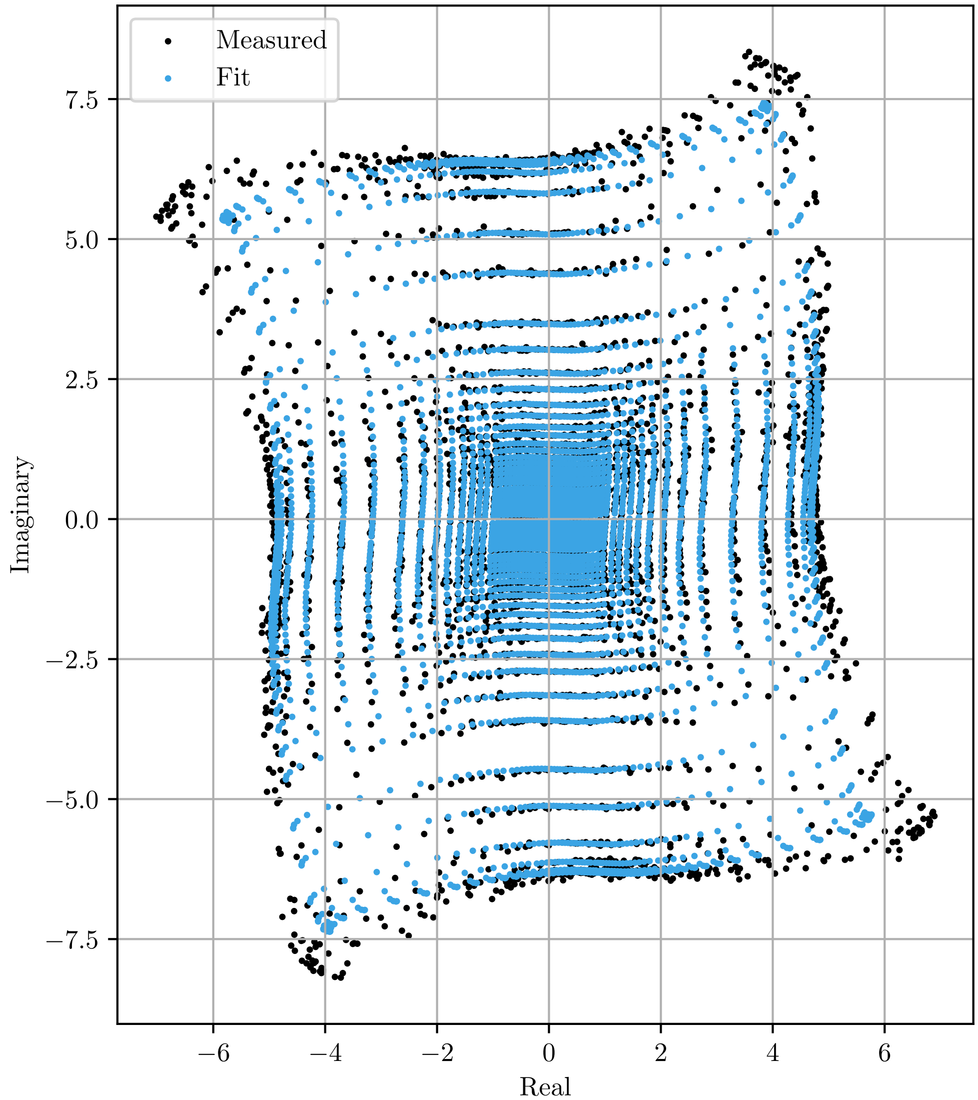

Figure 3.4: Measured ($\boldsymbol{T}^{\text{meas}}_{1,:,:}$) and fit ($\boldsymbol{T}^{\text{fit}}_{1,:,:}$) vector modulator settings for the first antenna element of the Sivers array.

in fact rarely used, if at all, in the quantization methods introduced next in Section 3.2. This process should be repeated for all antenna elements of the array, as they could possibly exhibit different behavior.

3.2 Quantization Threshold

The LUTs created in Section 3.1 characterize how a vector modulator's complex gain varies as a function of the i and q settings. While this is useful in mapping a beamforming vector $\boldsymbol{w}$ to actual settings, a necessary first step is to apply an appropriate scaling α to $\boldsymbol{w}$ to ensure it fits within the range of physically realizable weights. Since this scaling α is applied before quantizing the weight vector, it has a direct impact on which settings are chosen upon projecting via (3.1). To formalize this, without loss of generality, it is assumed that the designed beam weight vectors are scaled such that

$$\max_{n} |w_n| = 1, \tag{3.16}$$

i.e., the maximum amplitude of any of the weights is unity. In this case, each of the weights w_n would lie on or within the unit circle.

3.2.1 Fixed Quantization

Perhaps the simplest method to reliably scale $\tilde{\boldsymbol{w}}$ before projecting to discrete settings is to normalize it such that any given $|\tilde{w_n}|$ could never exceed the minimum magnitude of the outermost settings realizable by any of the N vector modulators. In other words, each scaled weight $\tilde{w}_n$ should be within the largest zero-centered circle inscribed in the convex hull of the LUT $\boldsymbol{T}$. Mathematically, this scaling α_{fix} can be expressed as

$$\alpha_{\text{fix}} = \underset{n \in [1,N],(i,q)\in\mathcal{B}}{\text{minimize}} \; |c_n T_{n,i,q}| \tag{3.17}$$

where $\mathcal{B}$ is the set of outermost points in the LUT:

$$\mathcal{B} = \{(0,q)\}_{q=0}^{M-1} \cup \{(M-1,q)\}_{q=0}^{M-1} \cup \{(i,0)\}_{i=0}^{M-1} \cup \{(i,M-1)\}_{i=0}^{M-1}. \tag{3.18}$$

This baseline approach makes sense in cases where all beam weights are the same amplitude, such as in conjugate beamforming. However, it is unnecessarily restrictive in other cases, where the weight of the element with the minimum outermost setting is nowhere close to the clipping point. This motivates the next method.

3.2.2 Maximum Calibrated Quantization

To make better use of a vector modulator's dynamic range, the approach in the previous section can be modified such that the amplitude of the weights of a desired beam $\boldsymbol{w}$ are taken into account. Specifically, $\alpha_{\max}$ can be designed by first scaling each element's part of the LUT by the weight to be applied, i.e.,

$$\alpha_{\max} = \underset{n\in[1,N],(i,q)\in\mathcal{B}}{\text{minimize}} \left|\frac{c_n T_{n,i,q}}{w_n}\right|, \tag{3.19}$$

guaranteeing that one of the chosen settings will be from the largest circle that fits within the LUT. As before, L_2 projection is used to select settings for a beam weight design via (3.1).

The difference between this quantization approach and the fixed quantization approach is illustrated in Figure 3.5. It can be seen that maximum calibrated quantization results in chosen settings that are further from the center, making better use of the vector modulator's dynamic range. These settings, therefore, result in beams with higher power, and permit accurate realization of beams that exhibit large dynamic range, such as those used in zero-forcing.

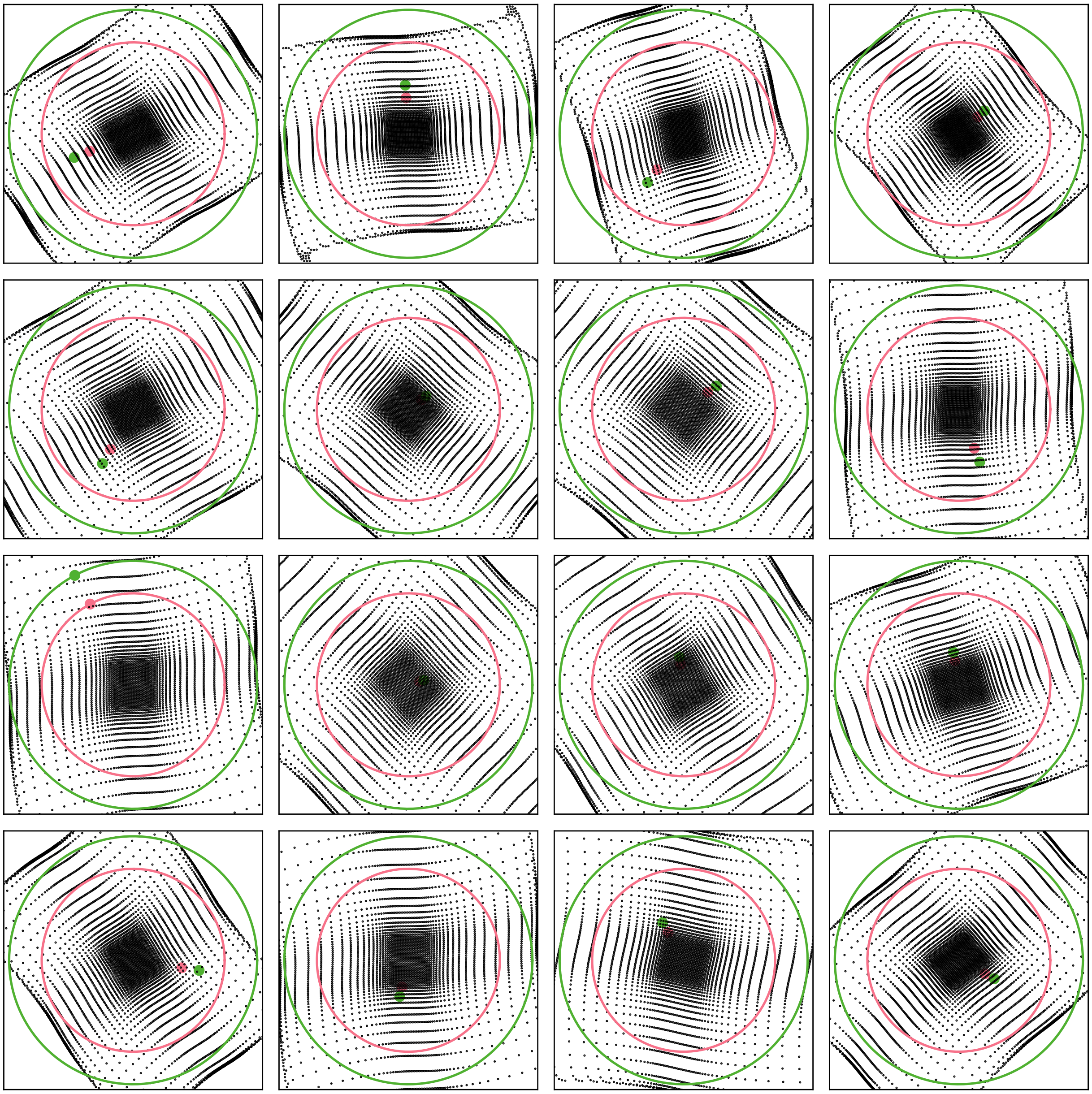

Figure 3.5: Comparison of the two quantization strategies, fixed (red) and maximum calibrated (green), for an array with $N = 16$ antennas. The values in the LUT $\boldsymbol{T}^{\text{fit}}$ for all $N = 16$ elements are shown in separate plots, along with each scaled weight $\tilde{\boldsymbol{w}}$ and the corresponding circle that it must fall within. Maximum calibration quantization makes better use of the vector modulators' dynamic ranges, producing beam realizations that are more accurate and have higher power.

CHAPTER 4

Measurement Setup & Methods

To develop and experimentally evaluate the proposed techniques from the previous chapter, a custom phased array platform and signal processing pipeline were used. Methods for measurement, calibration, and characterization of the phased arrays are described in this chapter, along with some select measurements.

4.1 Materials

The measurement platform fused a multitude of off-the-shelf components:

- 2 Sivers Semiconductors EVK6005 evaluation kits [53] equipped with BFM06010 beamforming modules [40].
- RFSoC4x2 development board from RealDigital [54], containing a system-on-chip with high-speed data converters, ARM processor cores, and programmable fabric.
- Desktop computer for additional data processing and storage.
- Antenna measurement turntable with stepper motor and Arduino controller.
- Mini-Circuits balun and splitter modules.
- SMA cables, connectors, and fixed attenuators.

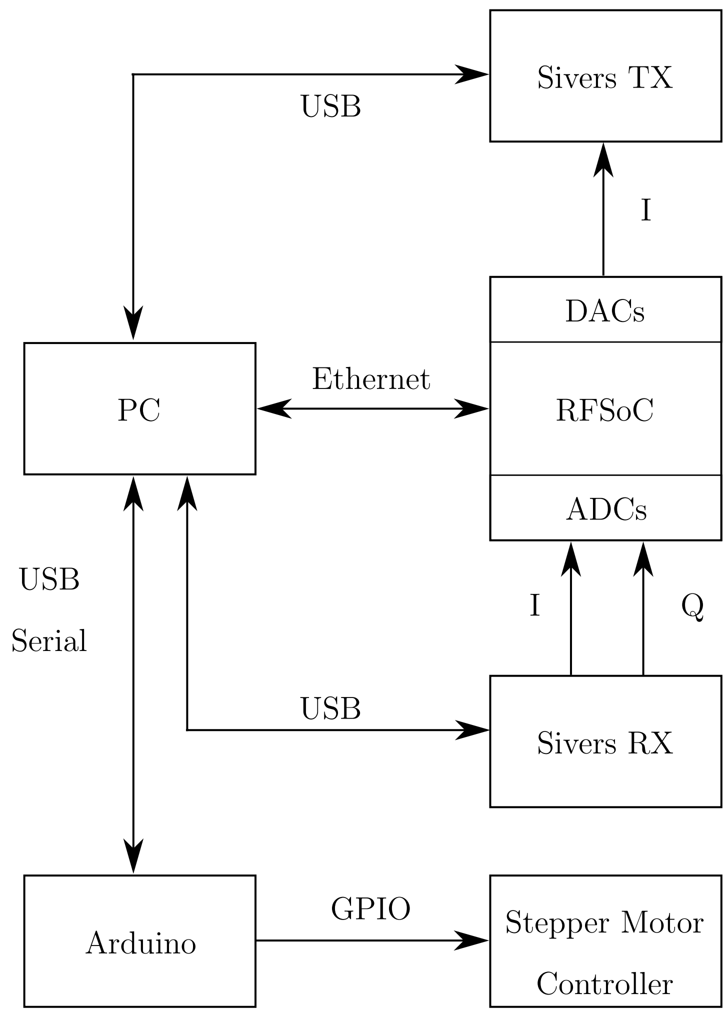

Figure 4.1: Functional block diagram of the measurement platform. The PC sends commands to the RFSoC, Sivers phased arrays, and Arduino over USB and Ethernet, and receives data from the RFSoC over Ethernet. The phased arrays are connected to the RFSoC's 4 GS/s data converters.

4.2 Setup Description

The phased array system consists of two units from Sivers Semiconductors, configured as a transmitter and receiver. These arrays are frequently used in experimental mmWave research [15, 43, 45, 46]. Each Sivers unit contains an RF front-end and beamformer. The input to the transmitter and the output of the receiver are both complex baseband differential signals (i.e., I-, I+, Q-, Q+) of up to 2 GHz of bandwidth. Each phased array module has $N = 16$ antenna elements arranged in a linear fashion and operates in the IEEE 802.11ad/ay (WiGig) band from 57–71 GHz. For the experiments in this thesis, the local oscillator (LO) frequency is configured to $f_\mathrm{c} = 60.48$ GHz, corresponding to IEEE 802.11ad/ay channel 2. Each antenna element's vector modulator has 6 bits of control for each of the I and Q paths, resulting in $2^{12} = 4096$ possible complex weight states.

Unless otherwise specified, the antenna arrays are placed facing each other and with enough separation such that near-field effects between the two are insignificant. Specifically, given the antenna arrays have an aperture of $D = 36$ millimeters and the wavelength is $\lambda_\mathrm{c} = 5$ millimeters, the arrays are placed such they lie in the Fraunhofer region [47]

$$d \geq \frac{2D^2}{\lambda_\mathrm{c}} \tag{4.1}$$

at a distance d of at least 0.52 meters.

The clock signal generated by the transmitter is fed into the receiver for synchronization using an SMA cable, which is necessary to avoid severe carrier frequency offset.

The setup leverages the RFSoC4x2 for high-speed data capture and processing. This board can be controlled with high-level Python commands through the PYNQ interface, with configurable FPGA fabric. On the RFSoC, synchronization between buffers transmitted through the digital-to-analog converters (DACs) and received through the analog-to-digital converters (ADCs) is achieved through multi-tile synchronization (MTS) [55]. The RFSoC's data converters can operate at 4 GS/s, and are connected to the Sivers arrays through SMA cables equipped with 1:1 baluns to generate a differential signal as required.

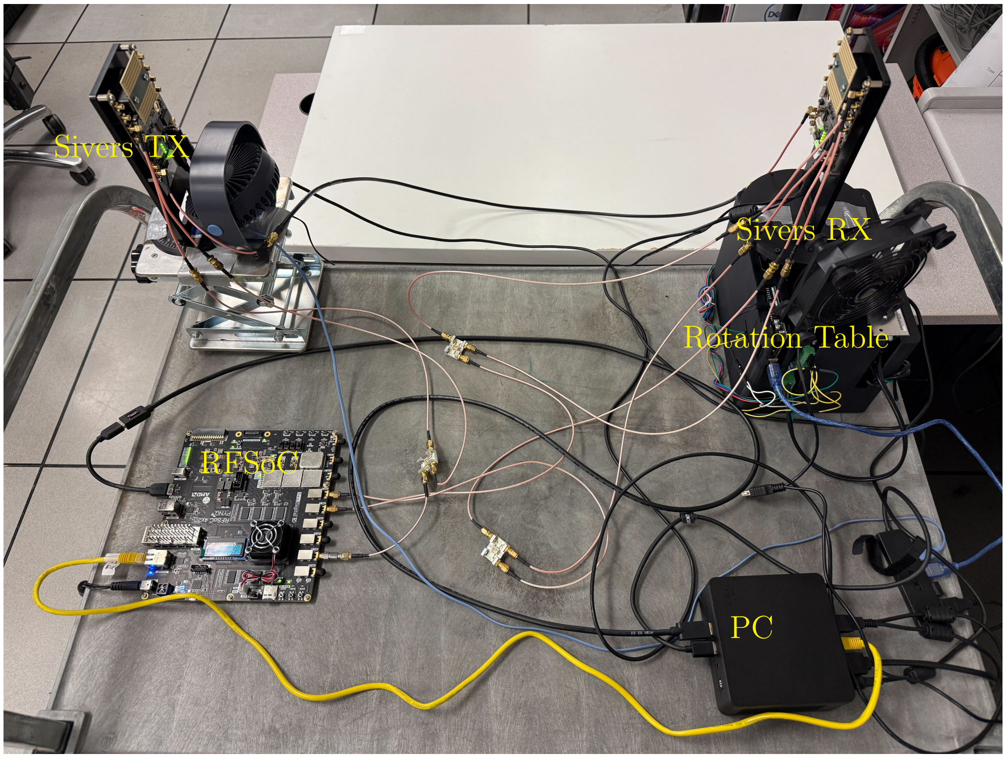

Figure 4.2: Labeled image of the phased array platform, configured to measure receive array's radiation pattern. Baseband signals are generated and received by the RFSoC, and all peripherals are connected to and controlled by a PC.

4.3 Coherent Complex Gain Measurement Procedure

Many of the measurements required later in this section are required to be *coherent*, meaning that both a magnitude and a phase are estimated. To take a coherent measurement, the RFSoC is configured such that the received signal is synchronized with an internal capture of the transmit signal. The following measurement and estimation scheme is used to take a complex gain measurement.

A single tone with exactly 2500 cycles is generated, which corresponds to a sinusoid of frequency $f_{\mathrm{d}} \approx 152.6$ MHz, since the RFSoC is configured to have an ADC sample rate of $f_{\mathrm{s}} = 4$ GS/s and to capture buffers of length $N_{\mathrm{s}} = 2^{16} = 65536$. This tone, expressed

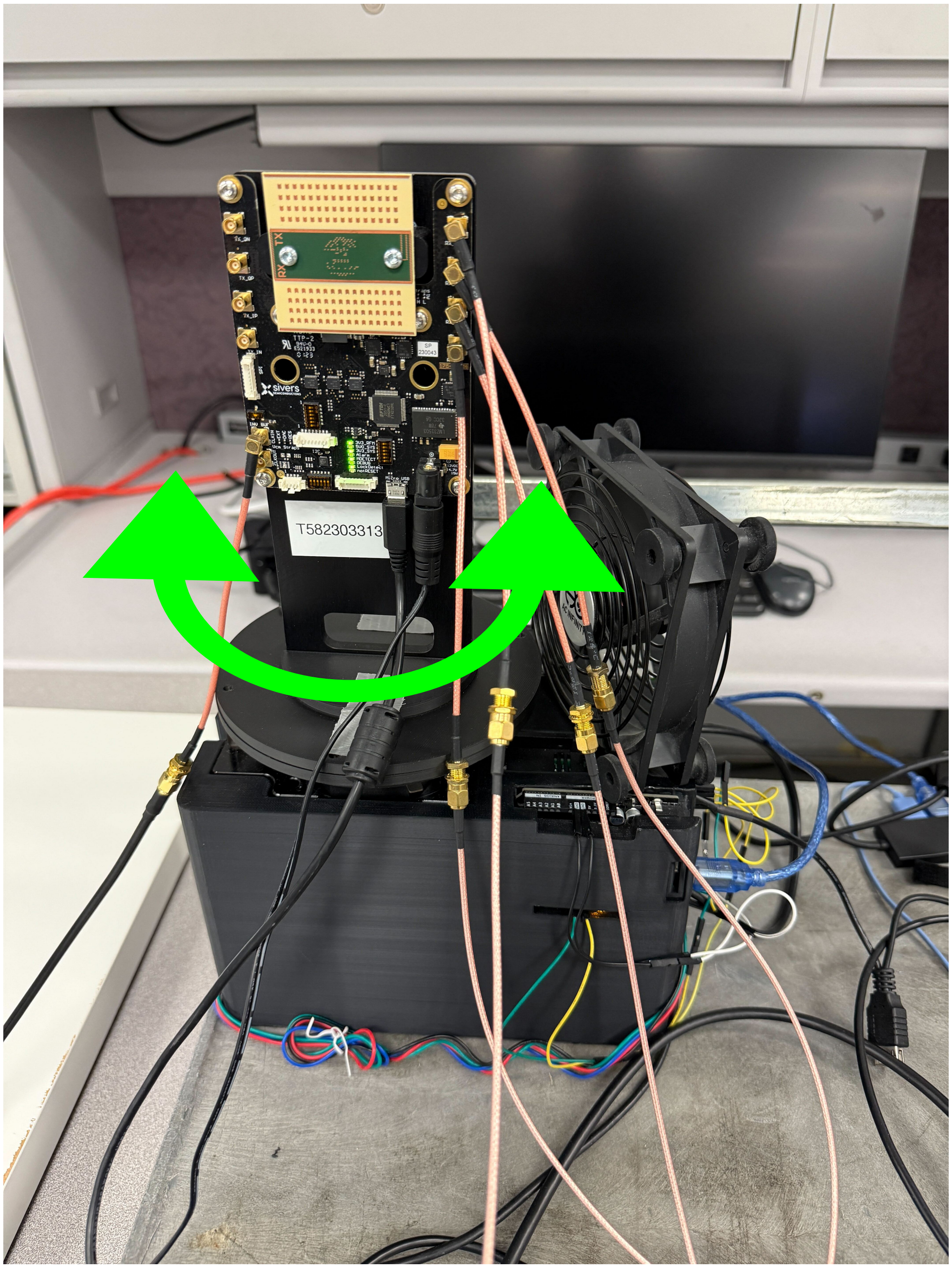

Figure 4.3: Image of the turntable setup, showing the axis of rotation. The table is rotated using a stepper motor controlled by an Arduino, connected to the main PC via USB serial.

mathematically as

$$x[n] = \mathrm{e}^{-\mathrm{j}2\pi \frac{f_\mathrm{d}}{f_\mathrm{s}} n}, \qquad n = 0, 1, \ldots, N_\mathrm{s} - 1, \tag{4.2}$$

is stored in memory. This tone is then cyclically transmitted by the DAC, which also performs an internal capture, expressed as

$$y_{\mathrm{t}}[n] = x[(n - L_{\mathrm{t}}) \mod N_{\mathrm{s}}], \qquad n = 0, 1, \ldots, N_{\mathrm{s}} - 1, \tag{4.3}$$

where L_{t} is an unknown cyclic shift due to the capture time. After analog upconversion, transmission, and downconversion by the Sivers front-ends, the received signal is similarly

$$y_{\mathrm{r}} = \alpha x[(n - L_{\mathrm{r}}) \mod N_{\mathrm{s}}] + v[n], \qquad n = 0, 1, \ldots, N_{\mathrm{s}} - 1, \tag{4.4}$$

where $|g|$ is an unknown scaling factor, L_{r} is an unknown cyclic shift, and $v[n]$ is noise.

Complex gain g is composed of the real gain $|g|$ and a phase shift $\angle g = 2\pi \frac{f_{\mathrm{d}}}{f_{\mathrm{s}}}(L_{\mathrm{r}} - L_{\mathrm{t}})$ due to these unknown cyclic shifts, and can be directly estimated as

$$g = \frac{\sum_{n=0}^{N_{\mathrm{s}}-1} y_{\mathrm{r}}[n]x[n]}{\sum_{n=0}^{N_{\mathrm{s}}-1} y_{\mathrm{t}}[n]x[n]}, \tag{4.5}$$

which can be additionally interpreted as a complex ratio of the discrete Fourier transform (DFT) of $y_{\mathrm{r}}[n]$ and $y_{\mathrm{t}}[n]$ evaluated at the bin corresponding to f_{d}. This algorithm is implemented using NumPy and configured to use the OpenBLAS library for acceleration on the RFSoC's Arm Cortex-A53 processor.

This approach requires perfect phase coherence between the transmit and receive front-ends, but this is challenging in practice due to imperfect synchronization of their LOs. Additionally, commodity hardware such as the Sivers front-ends are not designed with long-term coherence in mind [56], and indeed, severe phase noise is observed. This phase noise is, however, observed to be zero mean, and can thus be averaged out across numerous measurements, at the expense of increased measurement duration.

Since the noise present across multiple measurements is dominated by phase noise, separate magnitude and phase averages are taken. Extra care needs to be taken such that the average phase does not wrap, so the circular mean over N_{p} samples is computed as

$$\angle \hat{g} = \operatorname{atan2}\left(\sum_{p=1}^{N_{\mathrm{p}}} \Im(g_p)), \sum_{p=1}^{N_{\mathrm{p}}} \Re(g_p) \right) \tag{4.6}$$

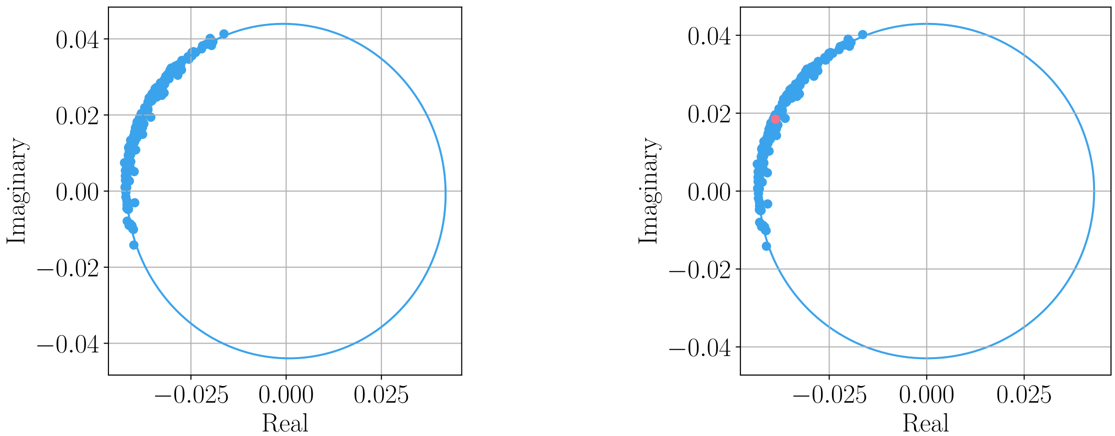

(a) Elliptical Fit

(b) Corrected Fit & Circular Mean

Figure 4.4: (a) 200 gain measurements of one particular vector modulator setting, with an ellipse fit to the data. (b) The same measurements after IQ correction, and the result of the averaging process. This process is repeated for each setting to be measured.

where g_p is the p-th gain sample.

Since the receiving Sivers array performs downconversion from 60 GHz to baseband, these measurements require an additional correction step. Imperfections in the receive chain and SMA cables can lead to the received I and Q channels experiencing slight gain and phase imbalance. This is an IQ imbalance (in the traditional sense), but it is important to note that it is distinct from and unrelated to the vector modulator IQ imbalance described in Chapter 2.

Since the test signal is unmodulated, typical pilot-based strategies for IQ estimation and correction cannot be applied. However, the repeated measurements experience the aforementioned phase noise, applying a rotation in the complex plane, so these different points can be fit to an ellipse using least squares to estimate the IQ imbalance. This process of joint IQ correction and phase noise averaging is shown in Figure 4.4.

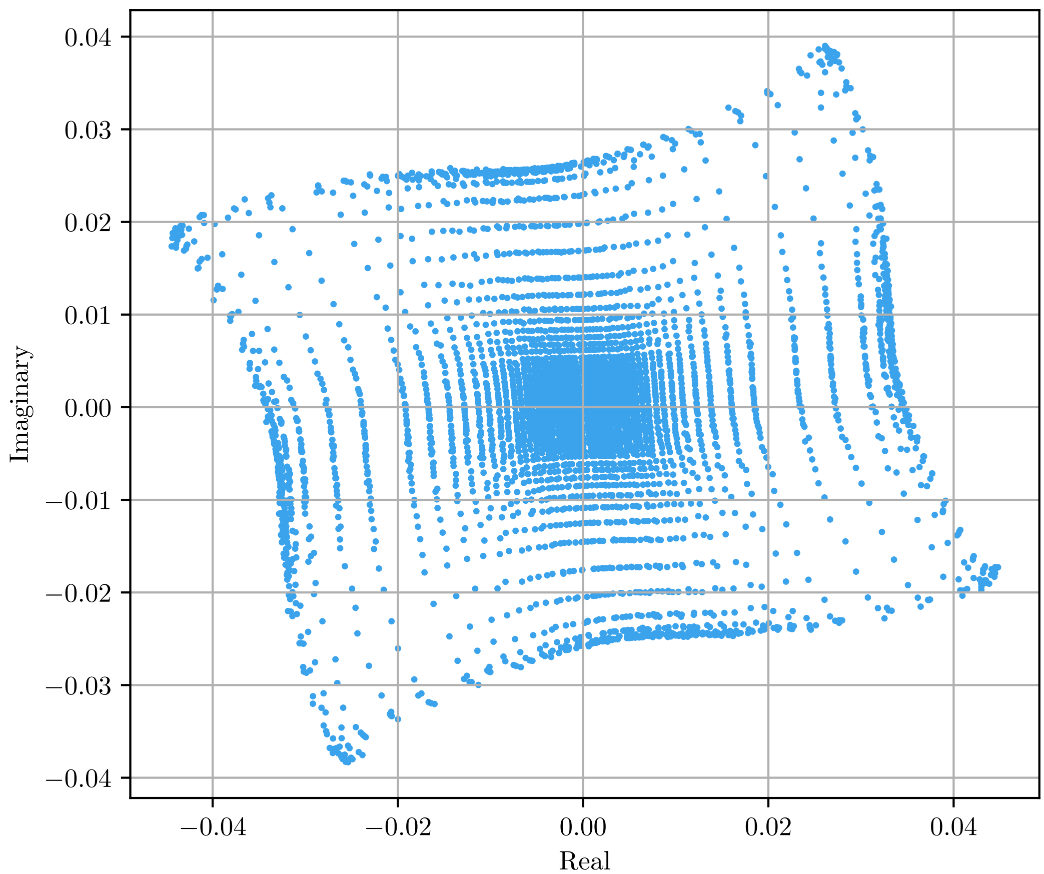

Figure 4.5: Measured complex states of all 4096 settings of the vector modulator at a single receive antenna element, after IQ imbalance correction and averaging.

4.4 Beam Setting Measurement

Full characterization of the phased array system requires measurement of every discrete realizable setting of each antenna element's vector modulator. To accomplish this, one array is tested at a time, with the other set to a constant configuration to complete the link. For instance, when testing the receive array, the transmit beam is set with one element activated and the rest maximally attenuated, acting as an approximately omnidirectional beam to illuminate the receive array. The receive beam is set similarly when testing the transmit array, so that the receiver can measure how the signal is attenuated and phase shifted as the transmit settings are changed. Since the magnitude and phase of each state must be measured, the coherent measurement approach discussed in Section 4.3 is used.

4.5 Radiation Pattern Measurement

Radiation patterns can be measured for both the transmit and receive array, with the other array acting as constant illumination, as before. For radiation pattern measurements, only power measurements are needed, so there is no need to average out the phase noise. The rotation table is used to sweep from $-60°$ to $60°$ in increments of $1°$. The same signal setup as in Section 4.3 is used, but the only the absolute value of the complex gain is used to calculate the relative power as $|g|^2$.

4.6 Array Manifold Measurement & Array Calibration

Directional beam design generally requires knowledge of the array geometry, including the exact array spacing d. As described in Section 2.3, the the miscalibration vector $\boldsymbol{c}$ and sometimes the element responses $e_n(\theta)$ are needed as well. Although the Sivers BFM06010 is known to be a ULA with microstrip patch antenna elements—which are identical and can be assumed to each have response $e(\theta)$—these exact details are not provided by the manufacturer. Thus, it is desirable to measure d, $\boldsymbol{c}$, and $e(\theta)$. All of these effects together can be represented as an element-wise version of (2.4), with the response of the n-th antenna element being modeled as

$$\tilde{a}(\theta, n, d) = e(\theta) \cdot c_n \cdot \mathrm{e}^{\mathrm{j}\frac{2\pi}{\lambda_\mathrm{c}}(n-1)d\sin(\theta)}, \qquad n = 1, 2, \ldots, N, \quad \theta \in \left[-\frac{\pi}{2}, \frac{\pi}{2}\right]. \tag{4.7}$$

Using the coherent measurement approach in Section 4.3 and measuring a few settings across various angles θ with the turntable, the array response $\tilde{\boldsymbol{a}}(\theta)$ can be measured. These measurements can then be fit to (4.7) using nonlinear least squares, using computational tools such as SciPy [57]. The extracted element spacing d for $f_\mathrm{c} = 60.48$ GHz is found to

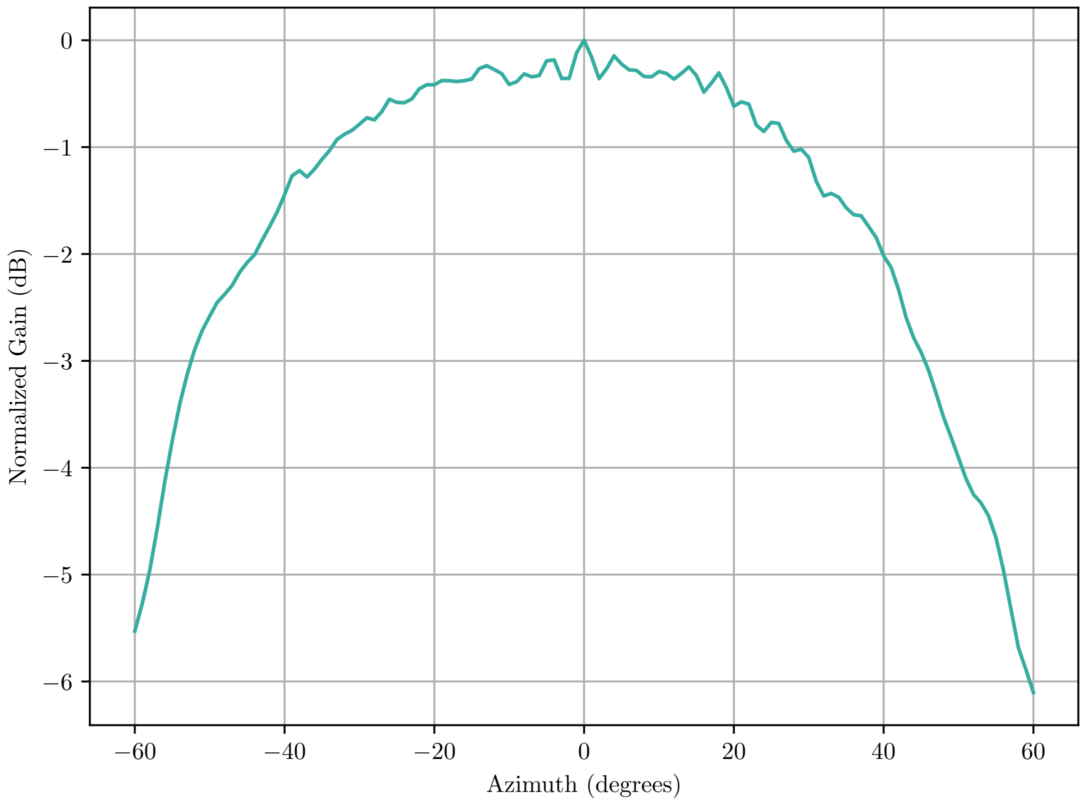

Figure 4.6: Combined element response $|e(\theta)|^2$ extracted from array manifold measurements.

be nearly a half-wavelength at $0.49\lambda_c$, and the extracted combined element response $e(\theta)$ is shown in Figure 4.6. An example of a measured beam with and without calibration accounted for is shown in Figure 4.7.

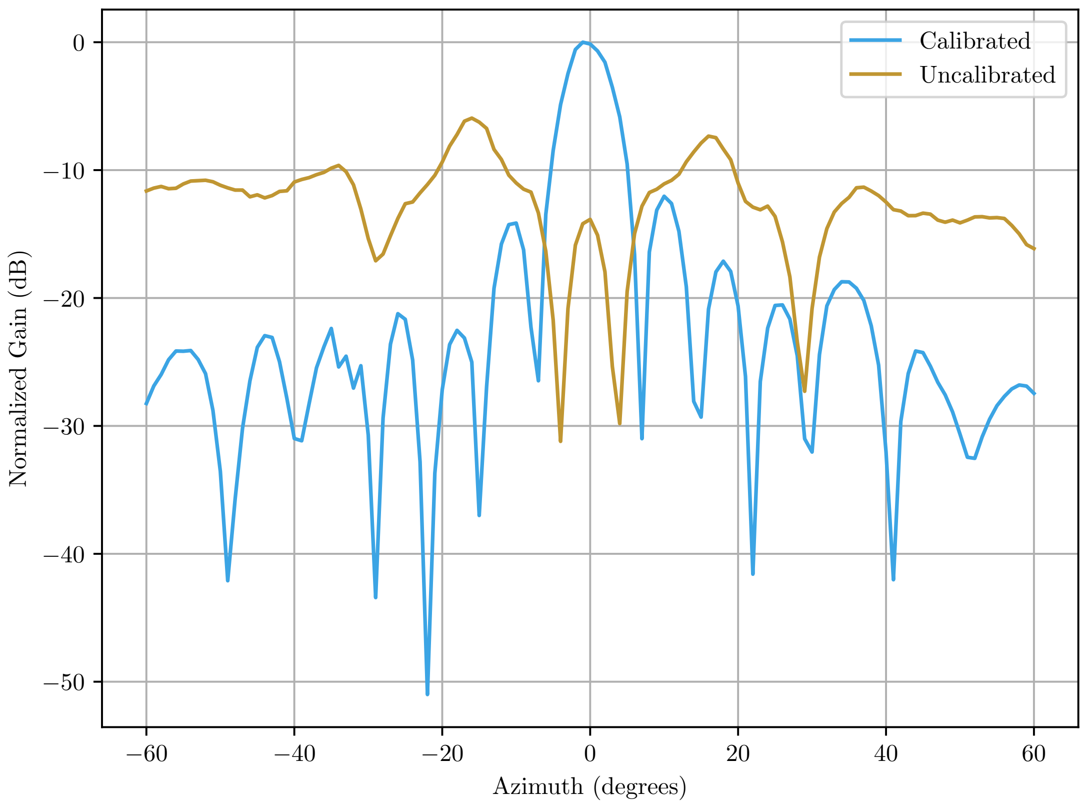

Figure 4.7: Measured boresight beam with and without calibration applied.

CHAPTER 5

Experimental Results

In this section, various beamforming techniques are experimentally evaluated. They are implemented on the hardware platform described in Chapter 4, using the methods presented in Chapter 3. The results are then analyzed and discussed.

5.1 Conjugate Beamforming

The simplest method for steering a beam in multi-antenna systems is conjugate beamforming, or matched filter beamforming, where power in a desired direction θ_{des} is maximized. This amounts to setting the beamforming weights equal to the array response as

$$\boldsymbol{w} = \boldsymbol{a}(\theta_{\text{des}}). \tag{5.1}$$

In conjugate beamforming, all elements in the weight vector $\boldsymbol{w}$ have the same amplitude, i.e., phase-only control is applied. As such, only fixed quantization is considered in this section, since max calibrated quantization brings no benefit when there are no amplitude differences across elements.

To assess the effectiveness of the strategies discussed in Chapter 3, radiation patterns of realized conjugate beams are measured and analyzed in terms of their main lobe gain and peak sidelobe level (PSL). For a given beam steered in a desired direction θ_{des}, PSL is defined as the maximum relative power exhibited by a beam outside of the main lobe, i.e.,

$$\text{PSL} = \frac{\max\limits_{\theta \notin [\theta_{\text{des}} - \frac{\Delta}{2}, \theta_{\text{des}} + \frac{\Delta}{2}]} G(\theta)}{G(\theta_{\text{des}})}, \tag{5.2}$$

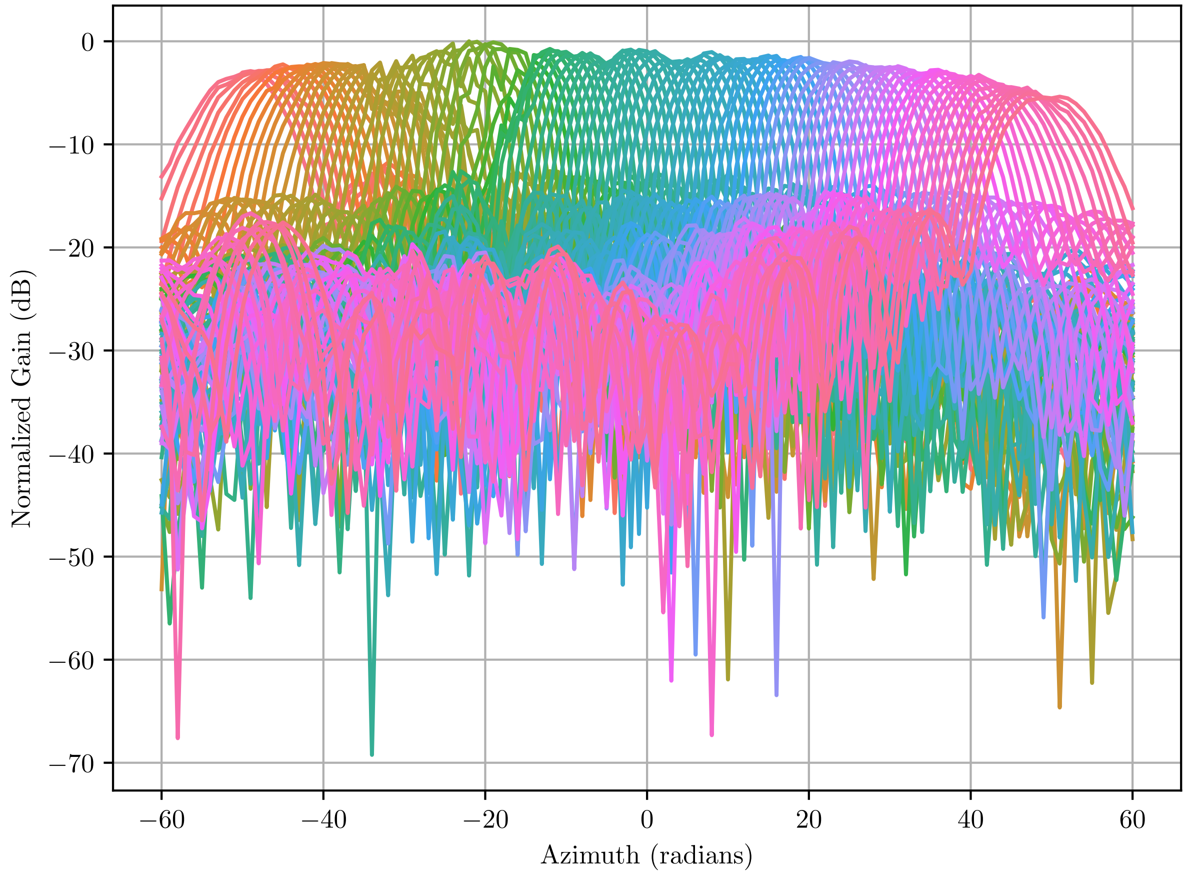

Figure 5.1: Measured radiation patterns for all 101 conjugate beams using the fit LUT.

where Δ is the main lobe width. In most applications, a low PSL is desirable, since it indicates a more directional radiation pattern and less power in undesired directions.

For testing purposes, 101 beams are realized using conjugate beamforming, steering from $-50°$ to $50°$ in increments of $1°$. An example of all 101 measured radiation patterns from a beam sweep are shown in Figure 5.1. This experiment is repeated for the linear, measured, and fit LUTs. Examples of conjugate beams realized these three ways are shown in Figure 5.2. In these particular cases, the beams generated with the measured and fit LUTs have visibly higher gain and lower sidelobes compared to those generated with the linear LUTs. Further evidence of this trend appears in Figure 5.3, which plots the empirical cumulative distribution

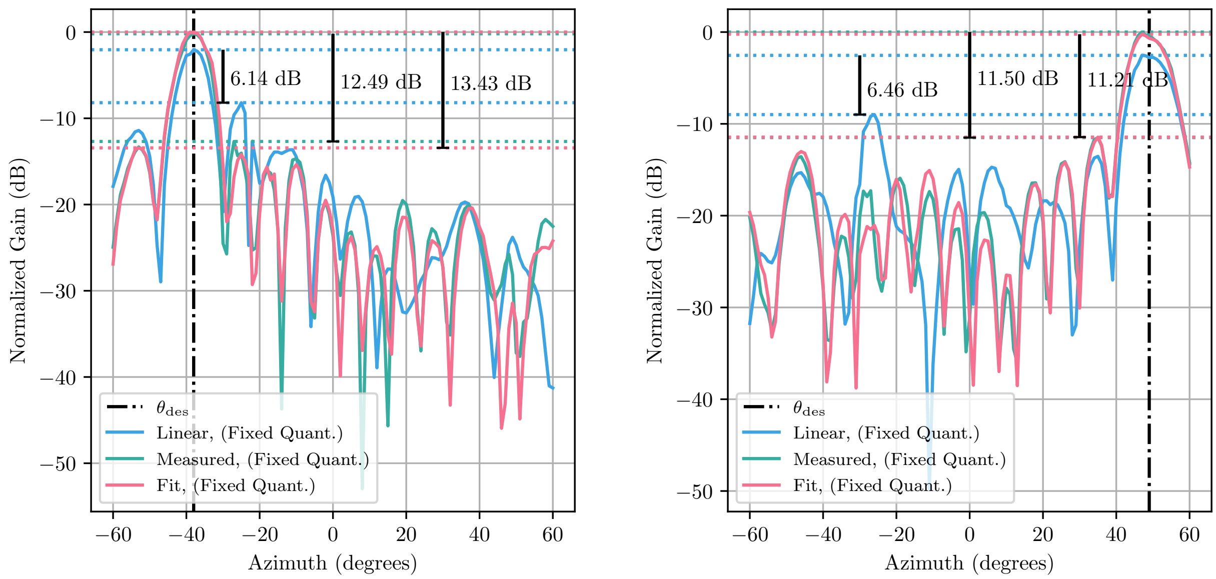

(a) $\theta_{\text{des}} = -39°$ (b) $\theta_{\text{des}} = 48°$

Figure 5.2: Two examples of conjugate beams, for (a) $\theta_{\text{des}} = -39°$ and (b) $\theta_{\text{des}} = 48°$, realized with linear, measured, and fit LUTs.

functions (ECDFs) of gain and PSL from all 101 measurements. This illustrates the merits of the measurement-based LUTs, even in the simple case of conjugate beamforming, compared to a simple linear LUT that ignores hardware nonidealities.

5.2 Taylor Beamforming

For many applications, it is desirable to design beams with explicitly low sidelobes, as to prevent/avoid unwanted interference outside of a main lobe direction. The most common way to do this is through apodization/windowing, i.e., applying tapered weights to a previously designed beam weight vector to suppress the sidelobe level [48]. This suppression comes at the expense of a wider main lobe but can provides useful isolation against interference or reflections from the environment. One window function frequently used in communications and radar for this purpose is the Taylor window [58,59]. The particular Taylor taper weights

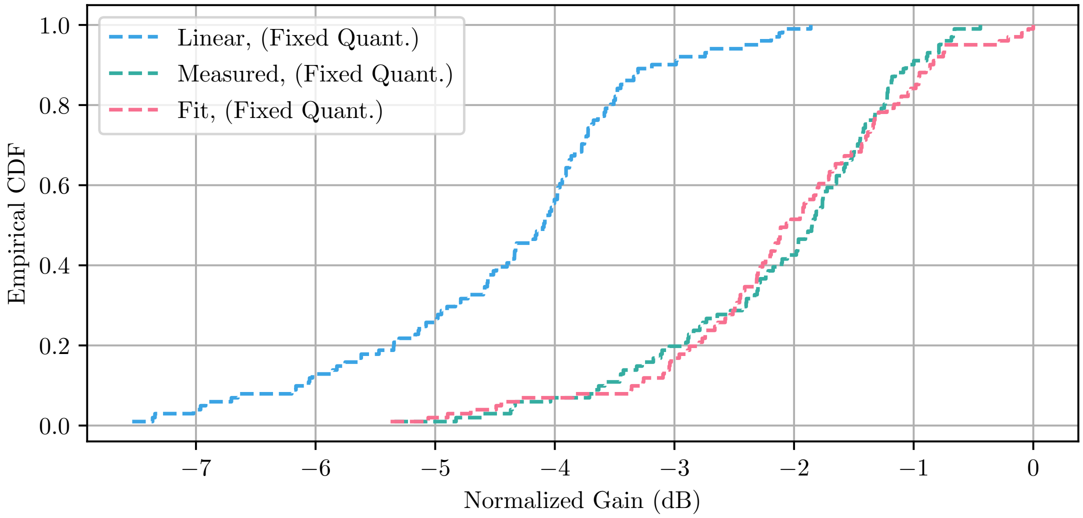

(a) Gain ECDF

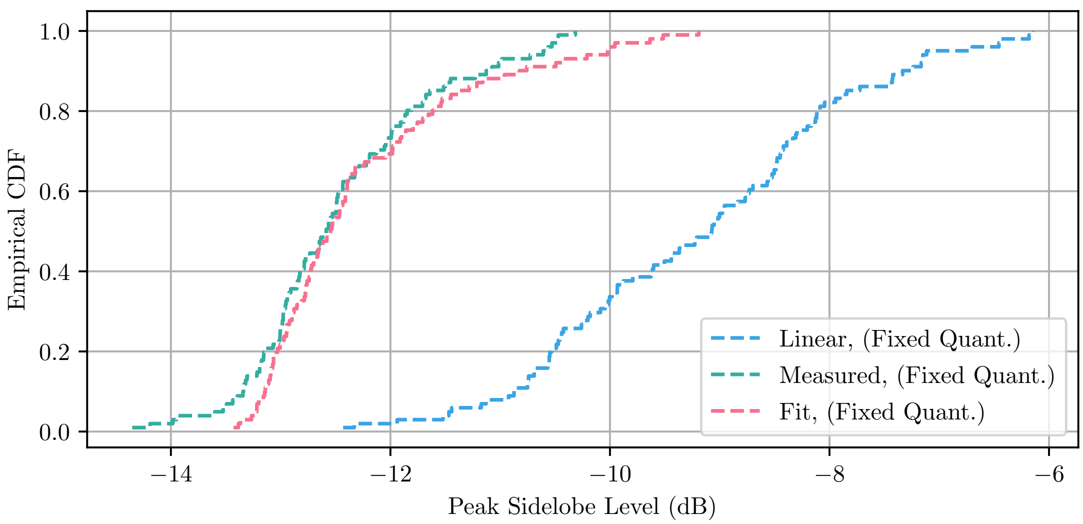

(b) PSL ECDF

Figure 5.3: ECDFs of conjugate beamforming (a) main lobe gain and (b) PSL for the three mapping strategies. Since the amplitude of beam weights in conjugate beamforming is equal across all elements, fixed quantization is applied.

used in this experiment are plotted in Figure 5.4, which are designed to exhibit a sidelobe suppression of 30 dB.

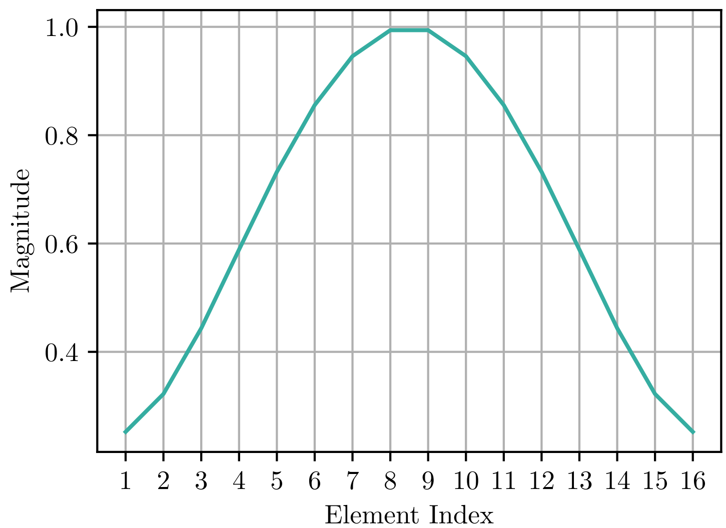

Figure 5.4: Taylor window with length $N = 16$ and desired sidelobe supression of 30 dB.

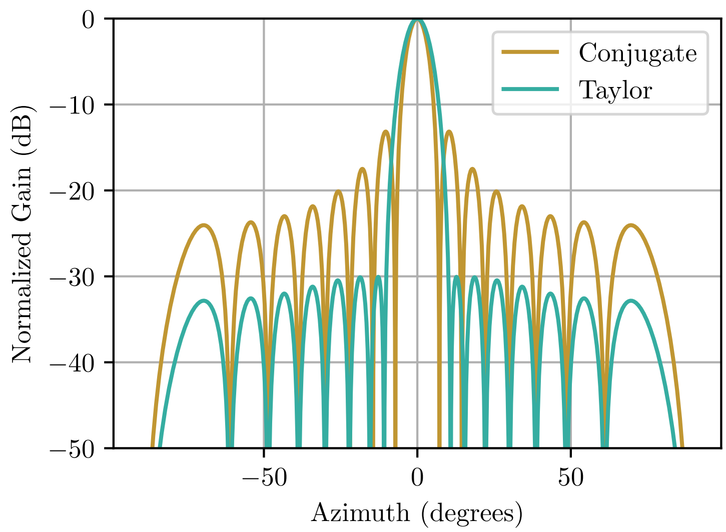

Figure 5.5: Simulated radiation patterns comparing conjugate beamforming and Taylor beamforming with desired sidelobe supression of 30 dB. As shown in the figure, Taylor beams have lower sidelobes compared to conjugate beams but also have a wider main lobe.

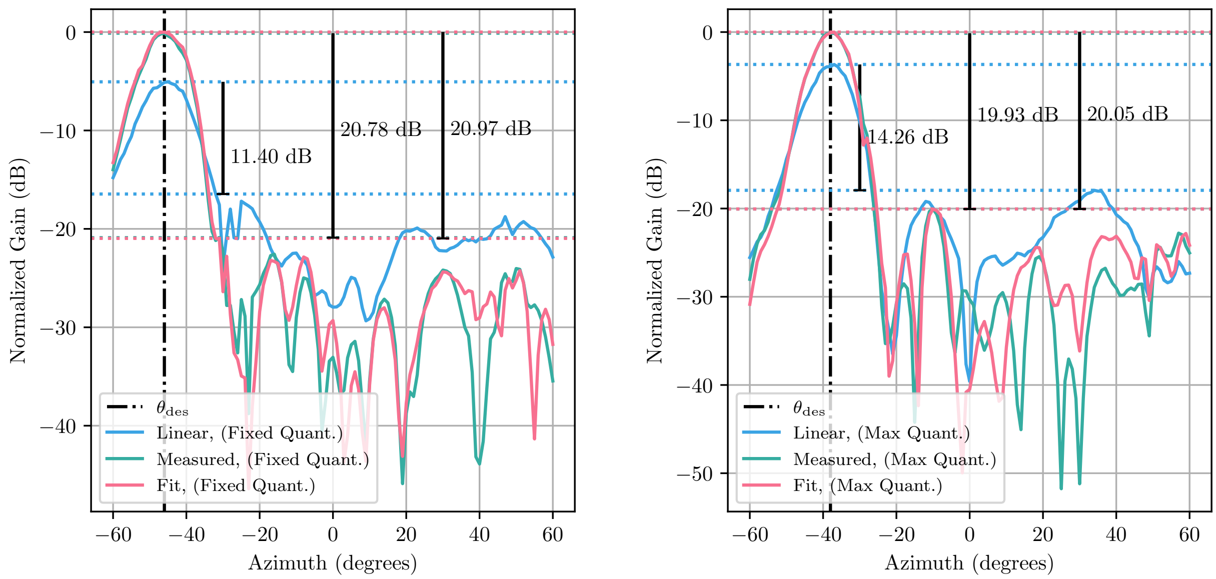

(a) $\theta_{\text{des}} = -56°$

(b) $\theta_{\text{des}} = -48°$

Figure 5.6: Two examples of Taylor beams, for (a) $\theta_{\text{des}} = -56°$ and (b) $\theta_{\text{des}} = -48°$, realized with linear, measured, and fit LUTs.

The experiment in Section 5.1 is repeated for the Taylor beamforming case, with both fixed and maximum calibrated quantization. Examples of Taylor beams measured this way are shown in Figure 5.6. As before, the ECDF of gain and PSL is shown in Figure 5.7. In this case, the benefits of max calibrated quantization and the measured LUTs are visible. The gain and PSL are comparable for the measured and fit LUTs, demonstrating that good, or perhaps even better, performance is possible without measuring every single setting. Max calibrated quantization also offers a gain boost of at least 1 dB.

Interestingly, max calibrated quantization had higher sidelobe levels for the linear LUT compared to fixed quantization. This can be explained by the fact that higher-amplitude settings are more likely to be chosen, and these settings deviate the most from a linear assumption. In contrast, when both quantization methods are applied to the measured and fit LUTs, the performance is comparable, indicating that they more closely fit the real device

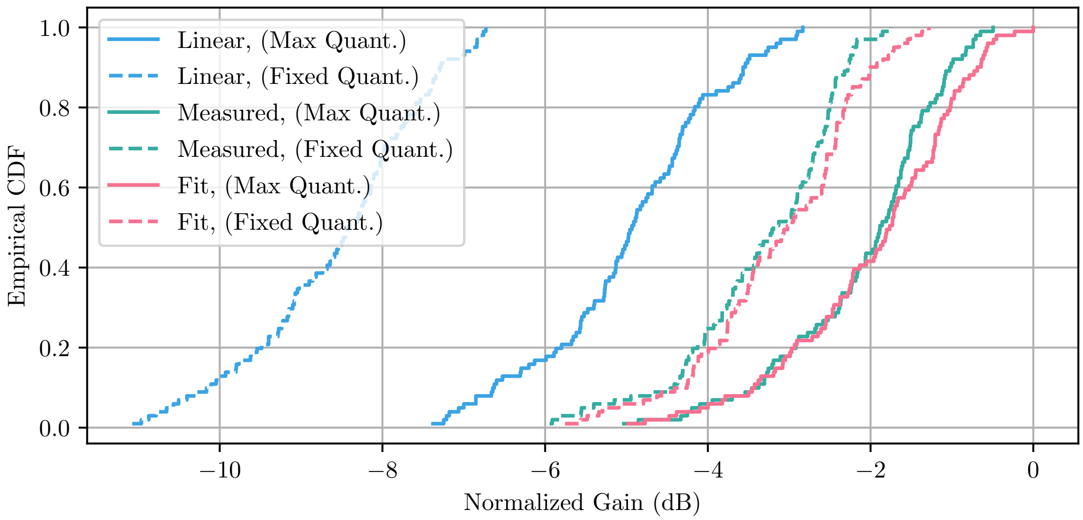

(a) Gain ECDF

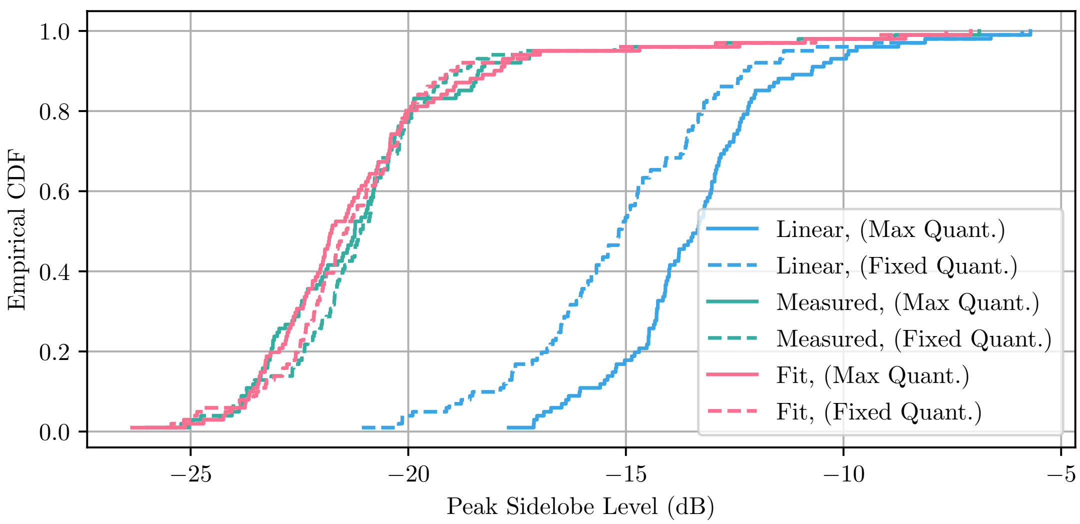

(b) PSL ECDF

Figure 5.7: ECDFs of Taylor beamforming (a) main lobe gain and (b) PSL for the three mapping strategies, for both fixed and max calibrated amplitude quantization.

behavior, even for high-amplitude settings.

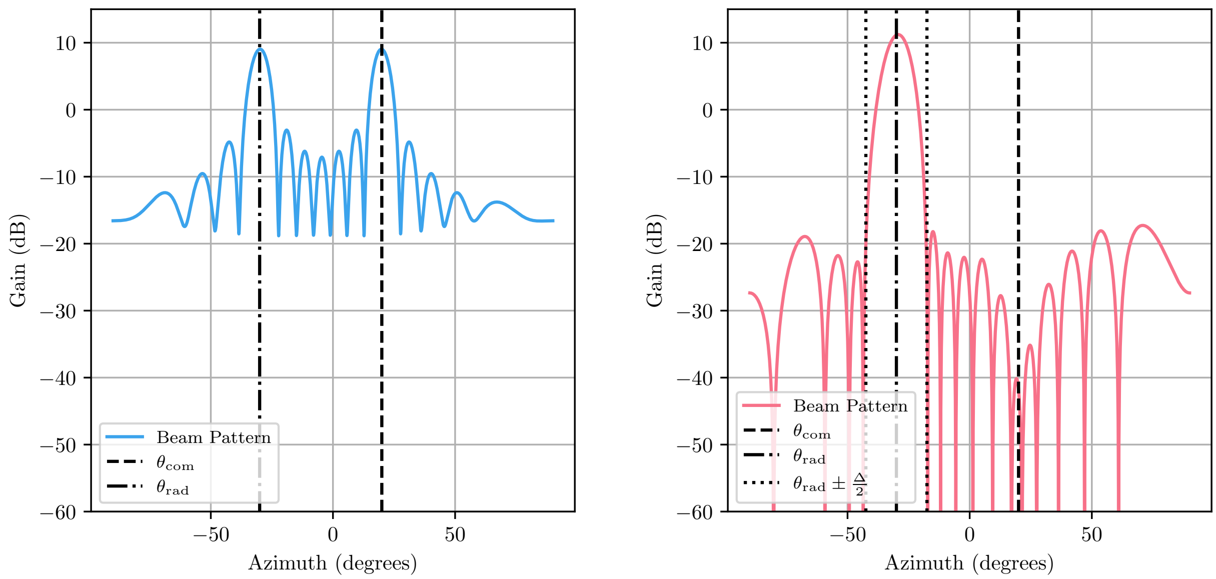

(a) Transmit radiation pattern

(b) Receive radiation pattern

Figure 5.8: Simulated (a) transmit and (b) receive radiation pattern plots of CPSL-optimized JCAS beams with $\theta_{\text{rad}} = -30°$, $\theta_{\text{com}} = 20°$, $\rho_{\text{com}} = 0.5$, and $\Delta = 30°$.

5.3 Combined Radar Pattern Optimization

One JCAS beamforming technique involves sending a transmission that both communicates with a user and illuminates a sensing direction of interest, while simultaneously receiving the reflections to perform the sensing task. In this scenario, it is necessary to design a transmit beamformer that maximizes power in two directions, namely a communication direction θ_{com} and a sensing direction θ_{rad}. A procedure for designing such a beam is discussed in [11]. First, array response vectors evaluated in the two directions are vertically stacked as

$$\boldsymbol{A}_{\text{tx}} = \begin{bmatrix} \boldsymbol{a}_{\text{tx}}(\theta_{\text{com}})^* \\ \boldsymbol{a}_{\text{tx}}(\theta_{\text{rad}})^* \end{bmatrix}. \tag{5.3}$$

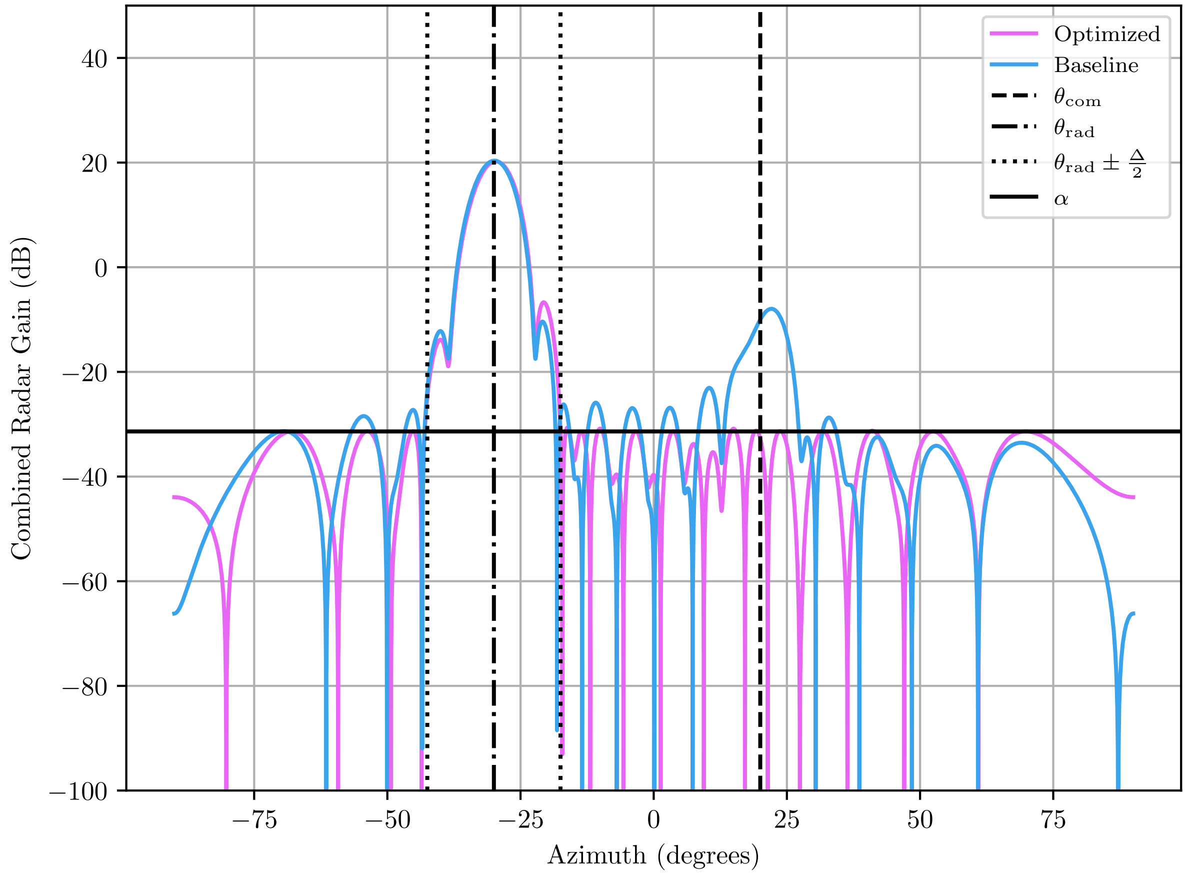

Figure 5.9: Simulated CRP plot of CPSL-optimized JCAS beams with $\theta_{\text{rad}} = -30°$, $\theta_{\text{com}} = 20°$, $\rho_{\text{com}} = 0.5$, and $\Delta = 30°$ (the same as those individually plotted in Figure 5.8), compared to a conjugate beamforming baseline. The optimized solution has a 20 dB lower PSL, and several of the other sidelobes are lower as well.

The transmit beam weights $\boldsymbol{f}$ can then be designed as the sum of the zero-forcing beams in both directions, i.e.,

$$\boldsymbol{f} = \boldsymbol{A}_{\text{tx}}^{*}(\boldsymbol{A}_{\text{tx}}\boldsymbol{A}_{\text{tx}}^{*})^{-1} \begin{bmatrix} \sqrt{\rho_{\text{com}}} \\ \sqrt{1-\rho_{\text{com}}} \end{bmatrix} \tag{5.4}$$

where $\rho_{\text{com}} \in [0, 1]$ represents the fraction of power allocated to the communication beam, with the rest of the power allocated to the radar sensing beam.

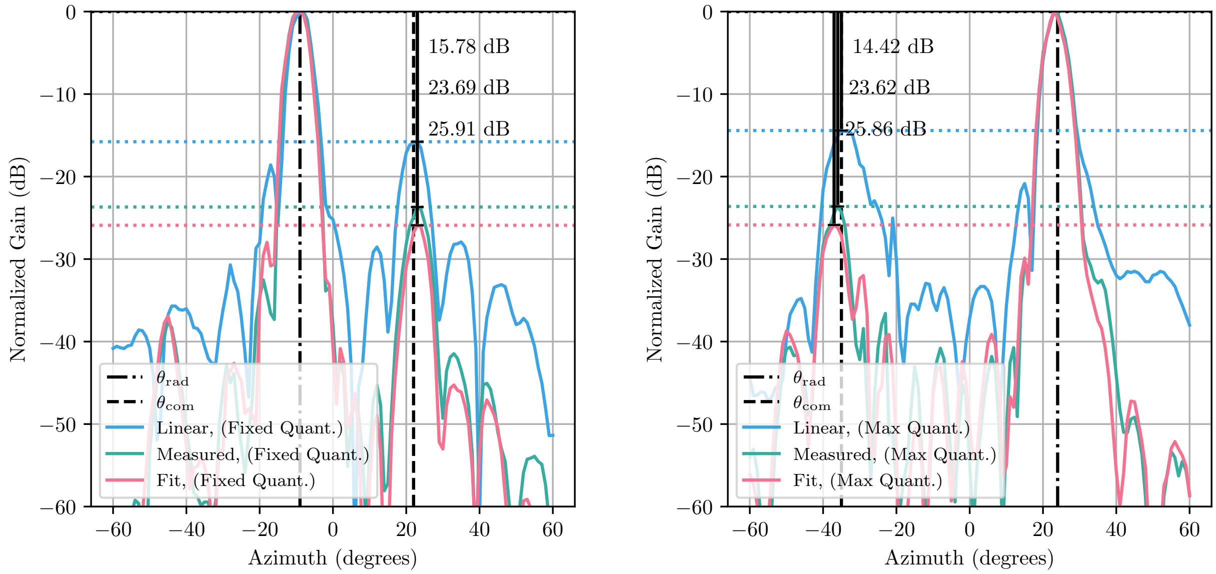

(a) $\theta_{\mathrm{rad}} = -9°$, $\theta_{\mathrm{com}} = 22°$, $\Delta = 20°$

(b) $\theta_{\mathrm{rad}} = 24°$, $\theta_{\mathrm{com}} = -35°$, $\Delta = 20°$

Figure 5.10: Two examples of CRPs for CPSL-optimized JCAS beams with various LUTs. Each beam is normalized so that its main lobe gain is 0 dB, so that the combined sidelobes can be easily compared.

In the JCAS setting, the transmission in the communication direction should have minimal effect on the receiver, as it could illuminate targets far away from the sensing direction. This can be harmful, as it can lead to false detections or mask weaker targets, limiting the overall dynamic range of the sensing system.

Recent work in JCAS beamformer design seeks to address this by optimizing the combined peak sidelobe level (CPSL) of the combined radar pattern (CRP) [11,16,60]. The combined radar pattern (CRP) is the multiplication of the transmit and receive radiation patterns, expressed mathematically as

$$G_{\mathrm{CRP}}(\theta) = G_{\mathrm{tx}}(\theta) \cdot G_{\mathrm{rx}}(\theta) \tag{5.5}$$

and represents the combined beamforming gain in a certain direction. For the sensing application, radio waves are emitted by the transmitter, reflected by targets and clutter, and are subsequently received at the receiver. As such, the CRP gain in a direction affects the strength of the received reflections. Because of this, it is desirable for the CRP to be high-gain in the sensing direction θ_{rad} (so that it amplifies target reflections) and low-gain in all other directions (so that clutter reflections from other parts of the scene are attenuated).

Optimization problems for this objective are formulated in [11,16,60], but are not convex [61], so this thesis instead considers a similar worst-case convex optimization problem

$$\min_{\alpha,\boldsymbol{w}} \quad \alpha \tag{5.6a}$$

$$\text{s.t.} \quad \max_{\theta}\left(|\boldsymbol{w}^*\boldsymbol{a}_{\text{rx}}(\theta)|\sqrt{G_{\text{tx}}(\theta)}\right) \le \alpha, \quad \theta \in \left[-90^\circ, \theta_{\text{rad}} - \frac{\Delta}{2}\right] \cup \left[\theta_{\text{rad}} + \frac{\Delta}{2}, 90^\circ\right] \tag{5.6b}$$

$$\boldsymbol{w}^*\boldsymbol{a}_{\text{rx}}(\theta_{\text{rad}}) = 1. \tag{5.6c}$$

This problem fixes the transmit beam $\boldsymbol{f}$ with gain $G_{\text{tx}}(\theta)$, and designs the receive beam $\boldsymbol{w}$ to minimize the maximum CRP outside of an interval around the main lobe, parameterized by Δ. The constraint $\boldsymbol{w}^*\boldsymbol{a}_{\text{rx}}(\theta_{\text{rad}}) = 1$ acts to create a beam with maximum gain in the sensing direction θ_{rad}. Since it is convex, this problem can easily be solved using computational tools such as CVXPY [62,63].

For illustration, simulated JCAS beams designed using these methods are shown in Figure 5.8. The CRP obtained from multiplying them is shown in Figure 5.9, along with a baseline using a conjugate receive beamformer, demonstrating how the CPSL can be significantly reduced using this method.

To experimentally evaluate the performance of the LUTs and quantization methods on this beamforming technique, 101 transmit and receive beam pairs are designed and implemented. These beam pairs are generated with θ_{rad} in 1° increments from -50° to 50°, and θ_{com} randomly selected from all values that are between -50° and 50° that also differ from θ_{rad} by at least 20°. $\Delta = 20^\circ$ is selected as the main lobe width for the optimization problem in (5.6).

Examples of CRPs from this experiment are shown in Figure 5.10, illustrating higher

CPSL when the linear LUT is used. All of the results are again plotted in Figure 5.11as ECDFs. Just as before, PSL performance of the fit LUT is similar to or slightly better than that of the measured LUT, far exceeding that of the linear LUT. The CRP gain is also higher when max calibrated quantization is used, rather than fixed quantization.

5.4 Null Steering

Another vital beamforming technique is *null steering*, where beams are designed to minimize (or completely eliminate) power in a given direction [64]. This is useful for reducing interference from other cooperative or uncooperative sources, canceling self-interference, and reducing the effect of the known reflectors in the environment. This section considers the zero-forcing approach, in which power is steered in a desired direction θ_{des}, while being minimized in one or more interference directions, the p-th of which is denoted by $\theta_{\text{int},p}$. An array response matrix for this case can be populated as

$$\boldsymbol{A}_{\text{rx}} = \begin{bmatrix} \boldsymbol{a}_{\text{rx}}(\theta_{\text{des}})^* \\ \boldsymbol{a}_{\text{rx}}(\theta_{\text{int},1})^* \\ \vdots \\ \boldsymbol{a}_{\text{rx}}(\theta_{\text{int},P})^* \end{bmatrix}, \tag{5.7}$$

and then a zero-forcing beam can be designed by taking the first column of the pseudoinverse of $\boldsymbol{A}_{\text{rx}}$ as

$$\boldsymbol{w} = \left[\boldsymbol{A}_{\text{rx}}^* (\boldsymbol{A}_{\text{rx}} \boldsymbol{A}_{\text{rx}}^*)^{-1}\right]_{:,1}. \tag{5.8}$$

In the results that follow, nulling a single direction θ_{int} is considered, but two additional nulls are placed at $\theta_{\text{int}} \pm 1°$ for increased robustness. In a manner similar to the CRP experiments, 101 beams are designed with θ_{rad} sweeping between $-50°$ and $50°$ in $1°$ increments, and θ_{int} randomly selected from values between $-50°$ and $50°$ that differ from θ_{rad} by at least $20°$. These beams are evaluated in terms of null depth, which is defined with respect to the

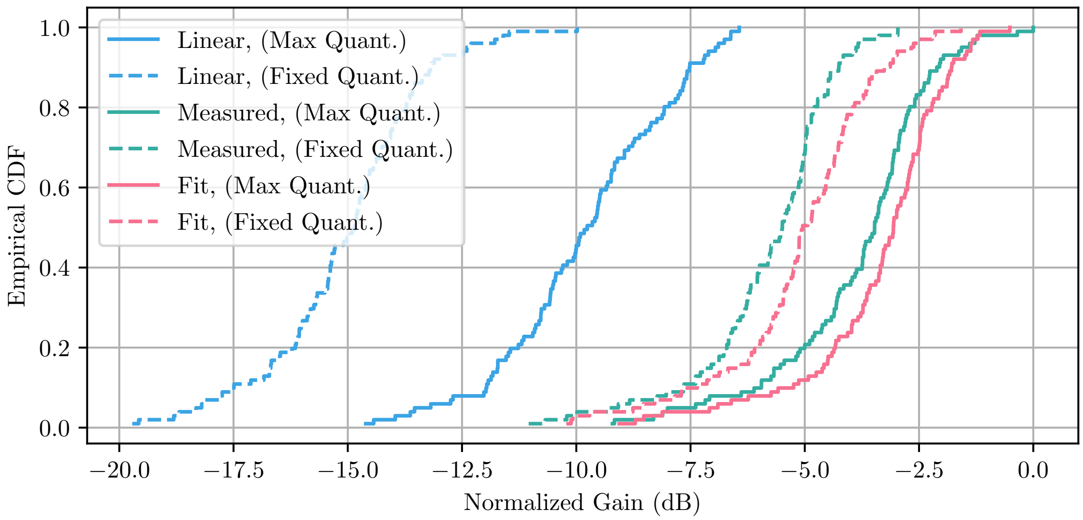

(a) Gain ECDF

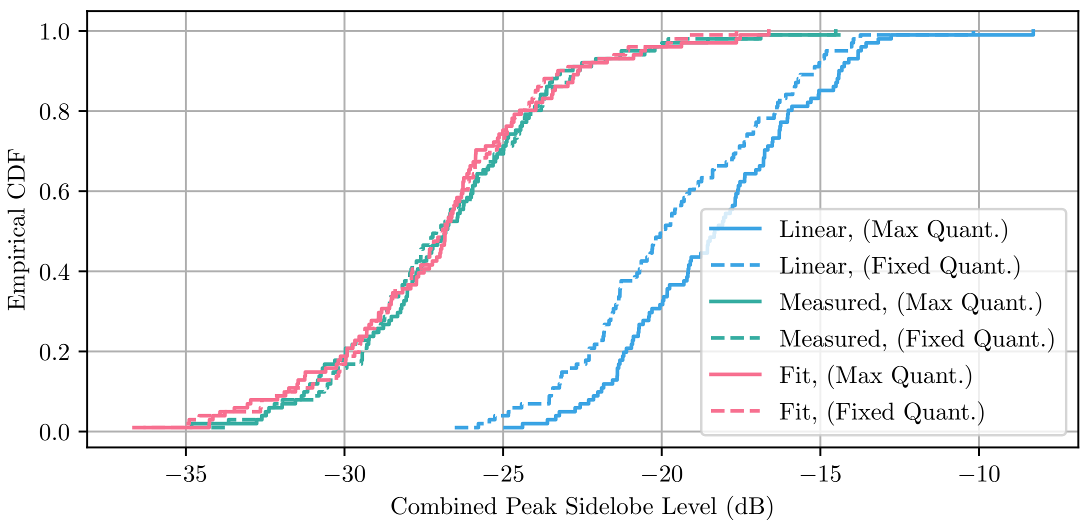

(b) PSL ECDF

Figure 5.11: ECDFs of JCAS beams, assessing (a) CRP gain and (b) CPSL for the three mapping strategies, for both fixed and max calibrated amplitude quantization.

main lobe gain as

$$\text{Null Depth} = \frac{G(\theta_{\text{des}})}{G(\theta_{\text{int}})}. \tag{5.9}$$

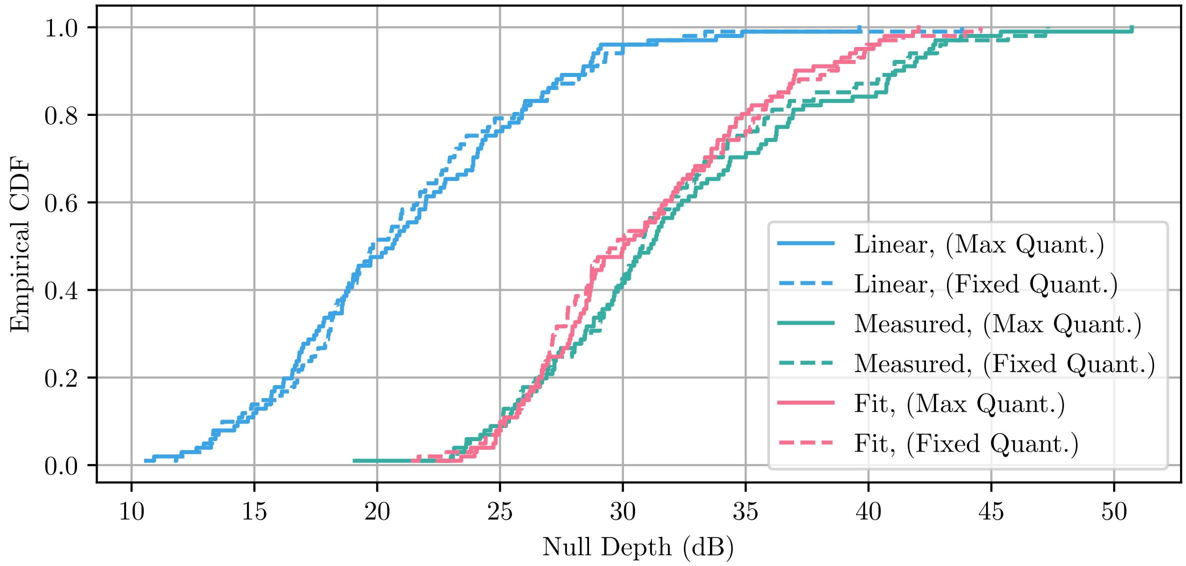

Figure 5.12: ECDF of null depth for the three mapping strategies, for both fixed and max calibrated amplitude quantization.

An ECDF of null depth across the various beam realizations is shown in Figure 5.12, illustrating the performance gap when an unrealistic linear assumption is made. As indicated by this figure, measurement data can be used to improve interference cancellation by 10 dB, which can be consequential in the presence of strong interference.

CHAPTER 6

Conclusion & Future Work

6.1 Conclusion

JCAS techniques often rely on crafting carefully designed beams, but this can be difficult to achieve on real-world mmWave arrays due to imperfections in the gain and phase control of each antenna element. This thesis addresses this challenge through a measurement and beam quantization framework. It is shown that measuring settings of vector modulator beamforming elements and characterizing them in terms of IQ imbalance, control nonlinearity, and gain-dependent phase variation can lead to better JCAS beam performance. Additionally, max calibration quantization is presented as a method for choosing vector modulator settings for a given beam such that the power is highest without eroding JCAS performance. These techniques are experimentally demonstrated on a phased array platform, which reveals improvements in main lobe gain, peak sidelobe level, and null depth—all of which can be decisive metrics in JCAS performance. These experimental methods also exhibit unprecedented control over the Sivers EVK06005 phased arrays, in particular, which serves as a useful contribution to the experimental mmWave research community in and of itself, given the wide use of these arrays in the literature.

6.2 Future Work

The work in this thesis motivates and paves the way for several interesting research directions in practical mmWave beamforming. For one, the behavior of vector modulators in this thesis is only considered at one frequency. It would be interesting to repeat measurements at multiple frequencies, to see how behavior varies. Analysis of this variance could be illuminating as to the source of the IQ imbalance and gain-dependent behavior, for instance.

While the techniques discussed in this work aim for better setting of beam weights, there is still a gap between simulated and real-world performance. It would be valuable to statistically analyze this remaining error, ideally expressing it in closed-form, and find additional ways to mitigate it.

In this work, beams are designed using a continuous set of weights and then projected onto discrete settings. While this is a sensible approach and proves effective, it is not necessarily optimal. A future research direction could seek to instead find the optimal discrete settings for a particular objective, rather than simply applying a projection. In other words, beams could be jointly designed and quantized to improve performance.

While the effect of oscillator phase noise on measurements can be addressed in the laboratory setting through repeated measurements, time is generally a more precious resource in real deployments. Future work could examine beam setting measurement methods that rely only on noncoherent (i.e., power-only) measurements. Compressive techniques, phase retrieval algorithms, and machine learning might be useful in this pursuit.

Lastly, many cutting-edge mmWave JCAS techniques in recent research literature have only been evaluated in simulation, so it would be valuable work to experimentally test the most promising ones. This line of work could lead to the development of novel beamforming techniques that directly take hardware into account, perhaps using models extracted from measurements or online learning methods that implicitly design beams that map well to a given hardware platform.

REFERENCES

[1] R. W. Heath Jr. and A. Lozano, *Foundations of MIMO Communication*. Cambridge, UK: Cambridge University Press, 2018.

[2] J. G. Andrews, S. Buzzi, W. Choi, S. V. Hanly, A. Lozano, A. C. K. Soong, and J. C. Zhang, "What will 5G be?" *IEEE J. Sel. Areas Commun.*, vol. 32, no. 6, pp. 1065–1082, Jun. 2014.

[3] V. Raghavan, J. Li, A. Sampath, O. Koymen, and T. Luo, *Millimeter Wave Communications in 5G and Towards 6G*. CRC Press, 2024.

[4] "Next G Alliance Report: Roadmap to 6G," Next G Alliance, Tech. Rep., Feb. 2022. [Online]. Available: https://www.nextgalliance.org/wp-content/uploads/2022/02/NextGA-Roadmap.pdf

[5] Nokia, "Transforming the 6G vision to action," Nokia, White Paper, Oct. 2025. [Online]. Available: https://www.nokia.com/asset/f/214027/

[6] "6G spectrum — enabling the future mobile life beyond 2030," Ericsson, Tech. Rep., Mar. 2023. [Online]. Available: https://www.ericsson.com/4953b8/assets/local/reports-papers/white-papers/6g-spectrum.pdf

[7] "6G — Connecting a cyber-physical world," Ericsson, Tech. Rep., 2022. [Online]. Available: https://www.ericsson.com/en/reports-and-papers/white-papers/a-research-outlook-towards-6g

[8] P. Kumari, J. Choi, N. González-Prelcic, and R. W. Heath, "IEEE 802.11ad-based radar: An approach to joint vehicular communication-radar system," *IEEE Transactions on Vehicular Technology*, vol. 67, no. 4, pp. 3012–3027, Sept. 2018.

[9] T. S. Rappaport, Shu Sun, R. Mayzus, Hang Zhao, Y. Azar, K. Wang, G. N. Wong, J. K. Schulz, M. Samimi, and F. Gutierrez, "Millimeter wave mobile communications for 5G cellular: It will work!" *IEEE Access*, vol. 1, pp. 335–349, May 2013.

[10] "Transforming industries with integrated sensing and communication," 5G Americas, Tech. Rep., 2025. [Online]. Available: https://www.5gamericas.org/transforming-industries-with-integrated-sensing-and-communication/

[11] C. B. Barneto, S. D. Liyanaarachchi, T. Riihonen, L. Anttila, and M. Valkama, "Multi-beam design for joint communication and sensing in 5G new radio networks," in *ICC 2020 - 2020 IEEE International Conference on Communications (ICC)*, 2020, pp. 1–6.

[12] Y. Luo, J. A. Zhang, X. Huang, W. Ni, and J. Pan, "Optimization and quantization of multibeam beamforming vector for joint communication and radio sensing," *IEEE Transactions on Communications*, vol. 67, no. 9, pp. 6468–6482, 2019.

[13] A. B. Gershman, N. D. Sidiropoulos, S. Shahbazpanahi, M. Bengtsson, and B. Ottersten, "Convex optimization-based beamforming," *IEEE Signal Process. Mag.*, vol. 27, no. 3, pp. 62–75, May 2010.

[14] J. Choi, J. Park, N. Lee, and A. Alkhateeb, "Joint and robust beamforming framework for integrated sensing and communication systems," *IEEE Transactions on Wireless Communications*, vol. 23, no. 11, pp. 17 602–17 618, 2024.

[15] H. Guo, R. Shen, F. Kosterhon, and Y. Ghasempour, "Panoptic: True joint mmWave communication and sensing with compressive sidelobe forming," *IEEE Journal on Selected Areas in Communications*, vol. 44, pp. 386–400, 2026.

[16] C. B. Barneto, T. Riihonen, S. D. Liyanaarachchi, M. Heino, N. González-Prelcic, and M. Valkama, "Beamformer design and optimization for joint communication and full-duplex sensing at mm-waves," *IEEE Transactions on Communications*, vol. 70, no. 12, pp. 8298–8312, 2022.

[17] C. B. Barneto, S. D. Liyanaarachchi, M. Heino, T. Riihonen, and M. Valkama, "Full duplex radio/radar technology: The enabler for advanced joint communication and sensing," *IEEE Wireless Commun.*, vol. 28, no. 1, pp. 82–88, Feb. 2021.

[18] I. P. Roberts, J. G. Andrews, and S. Vishwanath, "Hybrid beamforming for millimeter wave full-duplex under limited receive dynamic range," *IEEE Trans. Wireless Commun.*, vol. 20, no. 12, pp. 7758–7772, Dec. 2021.

[19] R. López-Valcarce and N. González-Prelcic, "Analog beamforming for full-duplex millimeter wave communication," in *Proc. ISWCS*, Aug. 2019, pp. 687–691.

[20] I. P. Roberts, S. Vishwanath, and J. G. Andrews, "LoneSTAR: Analog beamforming codebooks for full-duplex millimeter wave systems," *IEEE Trans. Wireless Commun.*, vol. 22, no. 9, pp. 5754–5769, Sep. 2023.

[21] Z. Gao, Z. Qi, and T. Chen, "Mambas: Maneuvering analog multi-user beamforming using an array of subarrays in mmwave networks," in *Proceedings of the 30th Annual International Conference on Mobile Computing and Networking*, ser. ACM MobiCom '24. New York, NY, USA: Association for Computing Machinery, 2024, p. 694–708. [Online]. Available: https://doi.org/10.1145/3636534.3649390

[22] O. M. Bakr and M. Johnson, "Impact of phase and amplitude errors on array performance," University of California, Berkeley, Tech. Rep. UCB/EECS-2009-1, Jan 2009. [Online]. Available: http://www2.eecs.berkeley.edu/Pubs/TechRpts/2009/EECS-2009-1.html

[23] S. Lee and H.-J. Song, "Accurate statistical model of radiation patterns in analog beamforming including random error, quantization error, and mutual coupling," *IEEE Transactions on Antennas and Propagation*, vol. 69, no. 7, pp. 3886–3898, 2021.

[24] E. Jaska, L. Corey, and S. Park, "Effects of random amplitude and phase errors on monopulse null depth in phased-array antennas," in *International Symposium on Antennas and Propagation Society, Merging Technologies for the 90's*, 1990, pp. 836–839 vol.2.

[25] H. Do and A. Lozano, "Optimum discrete beamforming via minkowski sum of polygons," 2025. [Online]. Available: https://arxiv.org/abs/2512.15546

[26] H. Do and A. Lozano, "Beamforming gain with nonideal phase shifters," 2026. [Online]. Available: https://arxiv.org/abs/2601.09426

[27] N. Borda, B. W. Domae, D. W. Browne, and D. Cabric, "Efficient RIS calibration and beamforming with discrete phase states," in *ICC 2025 - IEEE International Conference on Communications*, 2025, pp. 6826–6831.

[28] T. Moon, J. Gaun, and H. Hassanieh, "Online millimeter wave phased array calibration based on channel estimation," in *2019 IEEE 37th VLSI Test Symposium (VTS)*, 2019, pp. 1–6.

[29] M. K. Leino, J. Bergman, J. Ala-Laurinaho, and V. Viikari, "Beam optimization for 28 GHz phased array utilizing measurement data," in *2020 14th European Conference on Antennas and Propagation (EuCAP)*, 2020, pp. 1–5.

[30] M. Kebe, M. C. E. Yagoub, and R. E. Amaya, "A survey of phase shifters for microwave phased array systems," *International Journal of Circuit Theory and Applications*, vol. 53, no. 6, pp. 3719–3739, 2025. [Online]. Available: https://onlinelibrary.wiley.com/doi/abs/10.1002/cta.4298

[31] M. A. Alaei, A. B. J. Kokkeler, and P.-T. De Boer, "Vector modulator-based analog beamforming using the least euclidean distance criterion," *IEEE Access*, vol. 9, pp. 65 411–65 417, 2021.

[32] M. Y. Javed, N. Tervo, R. Akbar, B. Khan, M. E. Leinonen, and A. Pärssinen, "Improving Analog Zero-Forcing Null Depth with n-bit vector modulators in multi-beam phased array systems," in *2021 IEEE 93rd Vehicular Technology Conference (VTC2021-Spring)*, 2021, pp. 1–5.

[33] A. Sethi, R. Akbar, M. Hietanen, T. Rahkonen, and A. Pärssinen, "A 26GHz to 34GHz active phase shifter with tunable polyphase filter for 5G wireless systems," in *2021 16th European Microwave Integrated Circuits Conference (EuMIC)*, 2022, pp. 301–304.

[34] K. E. Drenkhahn, A. Gadallah, A. Franzese, C. Wagner, and A. Malignaggi, "A V-Band vector modulator based phase shifter in BiCMOS 0.13 µm SiGe technology," in *2020 15th European Microwave Integrated Circuits Conference (EuMIC)*, 2021, pp. 65–68.

[35] R. Arruela, D. M. Marinho, T. Varum, and J. N. Matos, "Design and characterization of an IQ reflection-type vector modulator for Ka-Band using PIN diodes," *IEEE Access*, vol. 8, pp. 212 855–212 864, 2020.

[36] Y. Chang and B. A. Floyd, "Reduction of phase and gain control dependencies within a 20 GHz beamforming receiver IC," *IEEE Access*, vol. 11, pp. 68 066–68 078, 2023.

[37] Y. Chen and S. Boumaiza, "Rapid calibration of variable gain phase shifters: A novel characterization approach with sparse measurements," in *2024 IEEE/MTT-S International Microwave Symposium - IMS 2024*, 2024, pp. 710–713.

[38] K. Greene, V. Chauhan, and B. Floyd, "Built-in test of phased arrays using code-modulated interferometry," *IEEE Transactions on Microwave Theory and Techniques*, vol. 66, no. 5, pp. 2463–2479, 2018.

[39] A. Mutapcic, S.-J. Kim, and S. Boyd, "Beamforming with uncertain weights," *IEEE Signal Processing Letters*, vol. 14, no. 5, pp. 348–351, 2007.

[40] "RF Module BFM06010 - Sivers Semiconductors," 2025. [Online]. Available: https://www.sivers-semiconductors.com/wireless/bfm06010/

[41] J. O. Lacruz, R. R. Ortiz, and J. Widmer, "A real-time experimentation platform for sub-6 GHz and millimeter-wave MIMO systems," in *Proceedings of the 19th Annual International Conference on Mobile Systems, Applications, and Services*, ser. MobiSys '21. New York, NY, USA: Association for Computing Machinery, 2021, pp. 427–439. [Online]. Available: https://doi.org/10.1145/3458864.3466868

[42] J. Pegoraro, J. O. Lacruz, T. Azzino, M. Mezzavilla, M. Rossi, J. Widmer, and S. Rangan, "Jump: Joint communication and sensing with unsynchronized transceivers made practical," *IEEE Transactions on Wireless Communications*, vol. 23, no. 8, pp. 9759–9775, 2024.

[43] I. P. Roberts, Y. Zhang, T. Osman, and A. Alkhateeb, "Real-world evaluation of full-duplex millimeter wave communication systems," *IEEE Trans. Wireless Commun.*, Mar. 2024.

[44] I. P. Roberts, Y. Zhang, T. Osman, and A. Alkhateeb, "Steer+: Robust beam refinement for full-duplex millimeter wave communication systems," in *Proc. Asilomar Conf. Signals, Sys., Comput*, Oct. 2023, pp. 134–139.

[45] Y. Zhang, T. Osman, and A. Alkhateeb, "Online beam learning with interference nulling for millimeter wave MIMO systems," Sep. 2022. [Online]. Available: https://arxiv.org/abs/2209.04509

[46] O. Delafrooz Noroozi, H. Guo, R. Shen, Z. Shao, H. Chen, K. Sengupta, Y. Ghasempour, and U. Madhow, "Zero-shot accurate mmwave antenna array calibration in the wild," in *Proceedings of the 30th Annual International Conference on Mobile Computing and Networking*, ser. ACM MobiCom '24. New York, NY, USA: Association for Computing Machinery, 2024, p. 1938–1945. [Online]. Available: https://doi.org/10.1145/3636534.3697323

[47] C. Balanis, *Antenna Theory: Analysis and Design*. Hoboken, New Jersey: John Wiley & Sons, 2016.

[48] W. L. Stutzman and G. A. Thiele, *Antenna Theory and Design*. John Wiley Sons, 1998.

[49] R. J. Mailloux, *Phased Array Antenna Handbook*. Norwood, MA, USA: Artech House, 2005.

[50] R. Sorace, "Phased array calibration," in *Proceedings 2000 IEEE International Conference on Phased Array Systems and Technology (Cat. No.00TH8510)*, 2000, pp. 533–536.

[51] B. Razavi, *RF Microelectronics (2nd Edition) (Prentice Hall Communications Engineering and Emerging Technologies Series)*, 2nd ed. USA: Prentice Hall Press, 2011.

[52] T. Schenk, *RF Imperfections in High-rate Wireless Systems: Impact and Digital Compensation*, 1st ed. Springer Publishing Company, Incorporated, 2008.

[53] "Evaluation kit EVK06005 - sivers semiconductors," 2025. [Online]. Available: https://www.sivers-semiconductors.com/wireless/evk06005/

[54] "RFSoC 4x2," 2026. [Online]. Available: https://www.realdigital.org/hardware/rfsoc-4x2

[55] G. Schelle and N. Jachimiec, "RFSOC-PYNQ Multi-Tile Synchronization Overlay," 2023. [Online]. Available: https://github.com/Xilinx/RFSoC-MTS

[56] M. E. Rasekh and U. Madhow, "Noncoherent compressive channel estimation for mm-wave massive MIMO," in *Proc. Asilomar Conf. Signals, Sys., and Comput.*, Oct. 2018, pp. 889–894.

[57] P. Virtanen, R. Gommers, T. E. Oliphant, M. Haberland, T. Reddy, D. Cournapeau, E. Burovski, P. Peterson, W. Weckesser, J. Bright, S. J. van der Walt, M. Brett, J. Wilson, K. J. Millman, N. Mayorov, A. R. J. Nelson, E. Jones, R. Kern, E. Larson, C. J.

Carey, İ. Polat, Y. Feng, E. W. Moore, J. VanderPlas, D. Laxalde, J. Perktold, R. Cimrman, I. Henriksen, E. A. Quintero, C. R. Harris, A. M. Archibald, A. H. Ribeiro, F. Pedregosa, P. van Mulbregt, and SciPy 1.0 Contributors, "SciPy 1.0: Fundamental algorithms for scientific computing in python," *Nature Methods*, vol. 17, pp. 261–272, 2020.

[58] T. Taylor, "Design of line-source antennas for narrow beamwidth and low side lobes," *Transactions of the IRE Professional Group on Antennas and Propagation*, vol. 3, no. 1, pp. 16–28, Jan. 1955.

[59] A. Doerry, "Catalog of window taper functions for sidelobe control," Sandia National Laboratories, Tech. Rep., Apr. 2017.

[60] A. Liu, T. Riihonen, and W. Sheng, "Full-duplex analog beamforming design for mm-wave integrated sensing and communication," in *2023 IEEE Radar Conference (RadarConf23)*, 2023, pp. 1–6.

[61] S. Boyd and L. Vandenberghe, *Convex Optimization.* Cambridge, UK: Cambridge University Press, 2004.

[62] S. Diamond and S. Boyd, "CVXPY: A Python-embedded modeling language for convex optimization," *Journal of Machine Learning Research*, vol. 17, no. 83, pp. 1–5, 2016.

[63] A. Agrawal, R. Verschueren, S. Diamond, and S. Boyd, "A rewriting system for convex optimization problems," *Journal of Control and Decision*, vol. 5, no. 1, pp. 42–60, 2018.

[64] S. Madani, S. Jog, J. O. Lacruz, J. Widmer, and H. Hassanieh, "Practical null steering in millimeter wave networks," in *18th USENIX Symposium on Networked Systems Design and Implementation (NSDI 21).* USENIX Association, Apr. 2021, pp. 903–921. [Online]. Available: https://www.usenix.org/conference/nsdi21/presentation/madani